

T-4068

DETERMINATION OF III-V SEMICONDUCTOR OPTICAL
CONSTANTS AND THEIR USE IN HIGH EFFICIENCY
SOLAR CELL OPTIMIZATION

by
Gregory S. Horner

ProQuest Number: 10783734

All rights reserved

INFORMATION TO ALL USERS

The quality of this reproduction is dependent upon the quality of the copy submitted.

In the unlikely event that the author did not send a complete manuscript and there are missing pages, these will be noted. Also, if material had to be removed, a note will indicate the deletion.



ProQuest 10783734

Published by ProQuest LLC (2018). Copyright of the Dissertation is held by the Author.

All rights reserved.

This work is protected against unauthorized copying under Title 17, United States Code
Microform Edition © ProQuest LLC.

ProQuest LLC.
789 East Eisenhower Parkway
P.O. Box 1346
Ann Arbor, MI 48106 – 1346

A thesis submitted to the Faculty and the Board of Trustees of the Colorado School of Mines in partial fulfillment of the requirements for the degree of Master of Science (Physics).

Golden, Colorado

Date 4/4/91

Signed: Gregory S. Horner
Gregory S. Horner

Approved: Don L. Williamson
Dr. Don L. Williamson
Thesis Advisor

Approved: Timothy J. Coutts
Dr. Timothy J. Coutts
Co-Thesis Advisor

Golden, Colorado

Date 4/5/91

John Trefny
Dr. John Trefny
Professor and Head,
Physics Department

Abstract

It is necessary to know the real and imaginary parts of the complex index of refraction ($N^* = N - ik$) of the materials in an optoelectronic device for proper design and performance optimization. This thesis discusses measurements of the optical constants of indium gallium arsenide (composition $\text{In}_{0.53}\text{Ga}_{0.47}\text{As}$), indium phosphide (InP) and indium gallium arsenide phosphide (composition $\text{In}_{0.25}\text{Ga}_{0.75}\text{As}_{0.54}\text{P}_{0.46}$). Two techniques, ellipsometry and reflection/transmission, have been used to determine $N^*(\lambda)$ of these materials over a much broader wavelength range than has been investigated thus far. A scanning ellipsometer has been developed which spans the visible-near infrared wavelength region from 360-1700 nm, thus enabling the first direct ellipsometric measurement of the NIR optical constants for the III-V alloys above. This information is used in conjunction with short circuit current optimization routines to design antireflection coatings (ARC's) for several types of high-efficiency solar cell, and devices are used to verify the results.

LIST OF FIGURES

<u>Figure</u>		<u>Page</u>
1	Bandgap vs. lattice constant for InGaAsP and AlGaAsSb	2
2	Band diagram for InP	5
3	Dielectric function of GaAs and numerical third derivatives	7
4	Definition of p and s polarization states	11
5	Illustration of polarizer and analyzer angles, P and A	14
6	Wavelength scanning ellipsometer: block diagram	20
7	Interference filter transmittance curves	22
8	Partial polarization fourier coefficients	23
9	Order sorting filter transmittance curves	25
10	Glan-Foucault and Rochon polarizer diagrams	28
11	$N^*(\lambda)$ for InP (ellipsometric results)	32
12	Comparison of figure 9 results with other published data	34
13	$N^*(\lambda)$ for $\text{In}_{0.53}\text{Ga}_{0.47}\text{As}$ (ellipsometric results)	35
14	$N^*(\lambda)$ for $\text{In}_{0.25}\text{Ga}_{0.75}\text{As}_{0.54}\text{P}_{0.46}$ (ellipsometric results)	37
15	Comparison of figure 11 results and reflectance/transmittance method	39
16	Determination of $\text{In}_{0.53}\text{Ga}_{0.47}\text{As}$ bandgap	41
17	Reflectance, transmittance, and diffuse transmittance of $\text{In}_{0.53}\text{Ga}_{0.47}\text{As}$	42
18	Global irradiance spectrum	45
19	Diagrams for interface and layer matrices	47
20	The total scattering matrix	53
21	Measured and modeled reflectance ($\text{In}_{0.25}\text{Ga}_{0.75}\text{As}_{0.54}\text{P}_{0.46}$)	57
22	J_{sc} contour plot for $^*\text{MgF}_2/^*\text{ZnS}/\text{MgF}_2(2 \text{ nm})/\text{InP}$	60

23	J_{sc} contour plot for *MgF ₂ */ITO/InP	61
24	Comparison of predicted and measured J_{sc} for *MgF ₂ */ITO/InP	62

ACKNOWLEDGEMENTS

I would like to thank all of the researchers in Dr. Tim Coutts' research group at DOE's Solar Energy Research Institute for their help in the work leading to this thesis. In particular, Xiaonan Li provided valuable assistance through preparation of the ITO/InP solar cells, and Ramesh Dhere directed the reflectance/transmittance measurements. The guidance of Fouad Abou-Elfotouh in the development of the scanning ellipsometer, and the provision of samples by Mark Wanlass are also acknowledged. Carl Osterwald and Don Dunlavy provided expert advice on the technical aspects of the ellipsometer development, and helped enormously in making the project a success. Jeff Wells also assisted in the development of the lengthy control code and calibration of the ellipsometer. Special thanks go to Tim Coutts for supporting me for the past three years.

This work was supported by NASA interagency order number C-3000-K and DOE contract number DE-AC02-83CH10093.

Table of Contents

	<u>Page</u>
ABSTRACT.....	iii
LIST OF FIGURES.....	iv
ACKNOWLEDGEMENTS.....	vi
Chapter 1. INTRODUCTION	
1.1 Scope and Purpose.....	1
1.2 Fresnel Equations.....	8
Chapter 2. ELLIPSOMETRY.....	12
2.1 Jones Representation of Polarized Light.....	13
2.2 Basic Equations of Ellipsometry.....	15
2.3 SERI UV-VIS-NIR Scanning Ellipsometer.....	19
2.3.1 Configuration.....	19
2.3.2 Monochromator.....	21
2.3.3 Detectors.....	24
2.3.4 Light Source.....	27
2.3.5 Polarizer and Analyzer.....	27
2.3.6 Computer Control.....	29
2.4 Ellipsometric Results.....	30
2.4.1 Indium Phosphide.....	31
2.4.2 Indium Gallium Arsenide.....	33
2.4.3 Indium Gallium Arsenide Phosphide.....	36
Chapter 3. REFLECTANCE/TRANSMITTANCE.....	38
Chapter 4. MODELING.....	43
4.1 Short Circuit Current Optimization.....	43
4.2 Scattering Matrix Method.....	46
4.2.1 Interface Matrix, I	46
4.2.2 Layer Matrix, L	50
4.2.3 Total Scattering Matrix for Coherent Lamella.....	52
4.3 Computer Implementation.....	55
4.4 Comparison of Measured and Modeled Reflectance.....	55

4.5	Modeling Results.....	56
Chapter 5.	CONCLUSIONS.....	63
.....		
	REFERENCES CITED.....	65

Chapter 1

INTRODUCTION

1.1. Scope and Purpose

Interest in the indium gallium arsenide phosphide (InGaAsP) family of semiconductor alloys has grown during the last 15 years in conjunction with a steady increase in the number of device applications. The technology of solid state lasers, LEDs, and optical communications equipment has advanced at an impressive pace, and basic materials studies continue to aid in the development of new applications. This thesis focuses on the development of a new ellipsometer which is used to directly study the near infrared optical properties of a select group of InGaAsP alloys.

$\text{In}_{1-x}\text{Ga}_x\text{As}_y\text{P}_{1-y}$ is lattice-matched to InP over a broad range of compositions and direct bandgaps ($E_g=0.73\text{-}1.35$ eV, figure 1) (1). In practice, this allows a device designer to tailor the material bandgap to a specific application while avoiding the additional complications caused by a lattice-mismatched system (2). For instance, optical fibers have been developed which exhibit minimum loss and dispersion in the near infrared, and the quaternary's fundamental absorption edge may be tailored to this region ($\sim 1.4\text{-}1.7$ μm) (3). The development of high-efficiency near infrared detectors and emitters remains a high priority in the communications industry.

Multiple-junction solar cells also require low bandgap, high efficiency bottom cells to effectively utilize the near infrared (NIR) portion of the incident spectrum (4), and recent SERI efforts have led to promising results. The direct bandgap materials

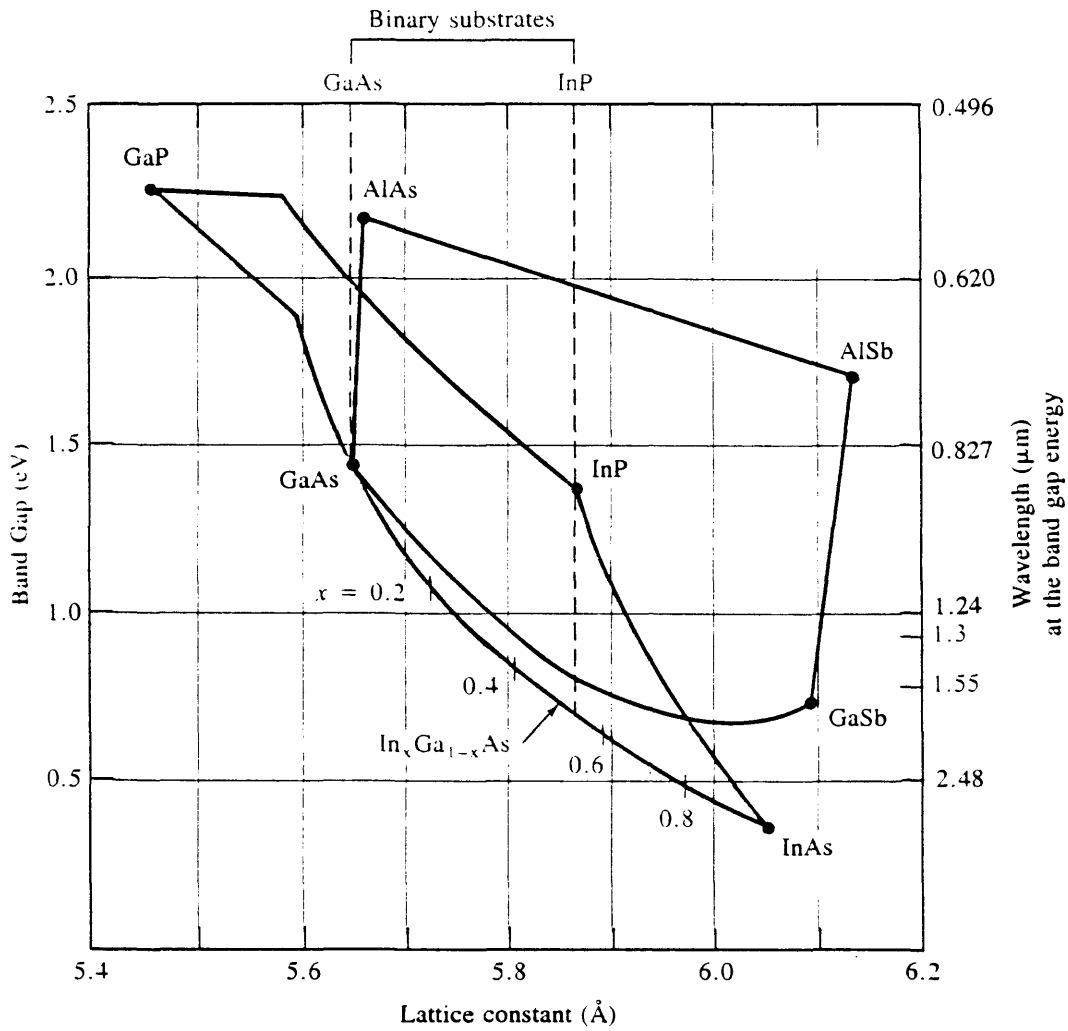


Figure 1. Band gap versus lattice constant for InGaAsP and AlGaAsSb. $\text{In}_{0.53}\text{Ga}_{0.47}\text{As}$ and $\text{In}_{0.25}\text{Ga}_{0.75}\text{As}_{0.54}\text{P}_{0.46}$ are lattice matched to InP substrates. Figure from reference 1, page 19.

$\text{In}_{0.25}\text{Ga}_{0.75}\text{As}_{0.54}\text{P}_{0.46}$ ($E_g=0.95$ eV), $\text{In}_{0.53}\text{Ga}_{0.47}\text{As}$ ($E_g=0.75$ eV), and InP ($E_g=1.35$ eV) have been used in these devices, and further optimization of the cells should lead to new efficiency records in the near future.

A major part of the optimization process for solar cells depends on accurate determination of the material optical constants, since efficiencies necessarily depend strongly on the amount of light which can be optically coupled into the cell. The process is, in part, one of simple impedance matching (5, 6). This is due to the fact that light travelling in a given (semi-infinite) medium is reflected from any other medium which exhibits a different index of refraction.

State of the art antireflection coatings, however, depend on coherent interference effects, rather than simple impedance matching. The light reflected from the front surface of a thin, planar structure (e.g.- a multi-layer solar cell) interferes (to varying degrees) either constructively or destructively with rays reflected from all material interfaces in the structure. Knowledge of the optical constants of all relevant materials allows the design of a cell which maximizes destructive interference over the operating wavelength range. Thus, light may be coupled quite efficiently into the structure, often with a reflectance of less than 2% over significant portions of the visible spectrum. In practice, application of a thin, transparent, double-layer antireflection coating may boost the efficiency rating of a solar cell by nearly fifty percent.

Beyond device optimization, the optical properties of a material give valuable insight into the basic material band structure. The optical constants may be couched in terms of either the standard index of refraction, $N^*=N-ik$, or the fundamental dielectric function, $\epsilon^*=\epsilon'+i\epsilon''$. The two quantities are related by the relations:

$$\epsilon' = N^2 - k^2$$

$$\epsilon'' = 2Nk$$

To see that the local dielectric function depends explicitly upon the band structure, note that it may be written as a function of the various interband momentum matrix elements and the k-space gradient of the interband energy in the independent-electron approximation (7):

$$\epsilon''(E) = \frac{\alpha}{E^2} \sum_{c,v} \int_{\mathcal{S}} d^2k \frac{|\hat{e} \cdot P_{cv}(k)|^2}{|\nabla_k E_{cv}(k)|}$$

where

$P_{cv}(k)$ = momentum matrix element.

$E_{cv}(k)$ = the 'interband energy,' $E_c(k) - E_v(k)$.

α = a constant

c, v = conduction and valence band states

e = unit polarization vector of incident light

The expression above may be derived from the random phase approximation, and it is valid over only small ranges of energy (hence the term 'local dielectric function').

Energies at which $\nabla_k E_{cv}(k) \rightarrow 0$ are called "critical point energies," and they are identified through structure in ϵ^* . The condition $\nabla_k E_{cv}(k) \rightarrow 0$ corresponds simply to parallel bands in momentum space, and it occurs at points of high symmetry (e.g.- Γ , L, X, figure 2) and where the conduction and valence bands remain parallel for significant ranges of momentum (e.g.- the E_1 transition, figure 2).

Figure 2 shows the results of a band structure calculation for InP. The E_0 (fundamental gap) and E_1 transitions have been labeled in the figure. The highest valence

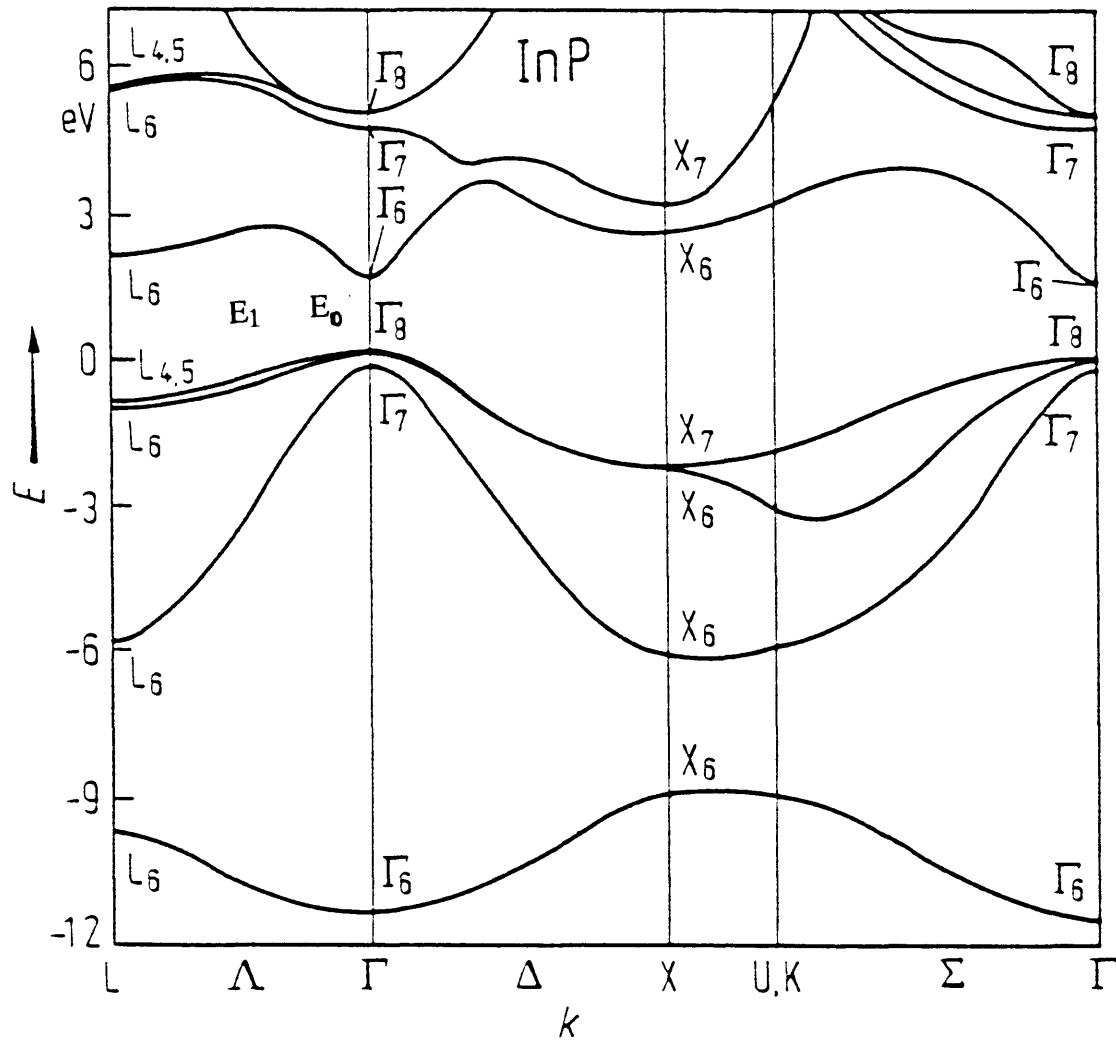


Figure 2. InP band diagram from Landolt-Bornstein II/17a, Semiconductors: Physics of Group IV Elements and III-V Compounds, with identification of the E_0 and E_1 transitions.

band is split in the $\Gamma \rightarrow L$ direction by spin-orbit coupling. This separates the E_1 transition into two components, usually denoted E_1 and $E_1 + \Delta_1$.

Probes of the dielectric function should be sensitive to effects such as spin orbit splitting if the band-to-band transition strengths are sufficiently large. For low-doped ($n \sim 1.0E16$) GaAs, spectral features have been correlated with band-to-band transitions (figure 3a). The features are broad, however, and they become even less distinct at higher doping levels (the case for most of the samples in this study). The slowly varying background may be suppressed with the use of numerical derivative techniques (figure 3b), allowing a more precise determination of the transition energy with complex Lorentzian lineshape analysis (5,7). The data in figure 3b are presented in the form of a third derivative of ϵ'' with respect to energy. This is done to facilitate comparison with the results of electromodulation techniques, which experimentally provide third derivative spectra through the application of a symmetry-breaking field (5,7). This formalism has allowed researchers to solve for critical point energies, phenomenological broadening parameters, and strengths of InGaAsP band-to-band transitions using measured dielectric functions (3).

Ellipsometric data is often used in fundamental physical studies due to its generally acknowledged status as the most accurate method for determination of optical constants (8, 9). In contrast to most optical techniques, which rely heavily on proper normalization of the detected signal, ellipsometry is a pure ratio technique (see chapter 2). Unfortunately, many studies have been limited to the analysis of band-to-band transitions located at energies greater than 1.5 eV, since no near infrared ellipsometric data have been presented in the literature (3).

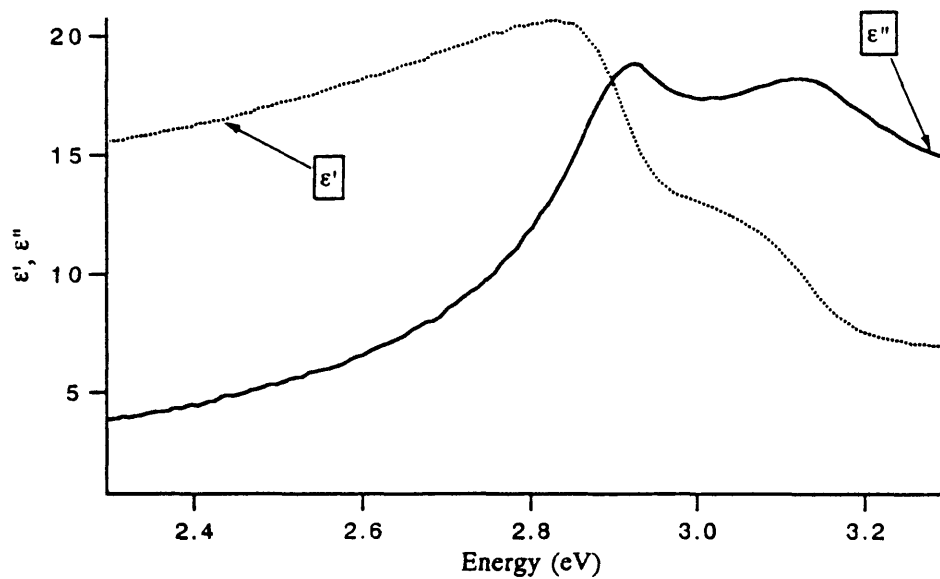


Figure 3a. Real and imaginary parts of the dielectric function for GaAs, as measured with the SERI wavelength scanning ellipsometer.

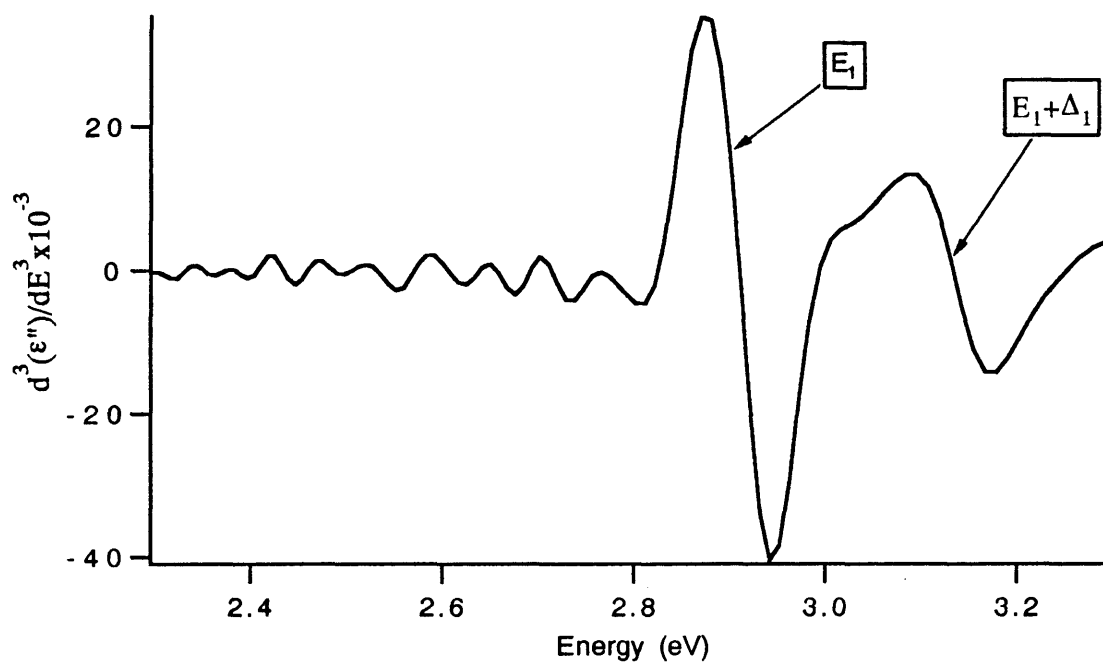


Figure 3b. Third derivative of the imaginary part of the dielectric function from figure 3a. The GaAs E_1 and $E_1 + \Delta_1$ transitions are visible.

This thesis presents the results obtained with a new, near infrared ellipsometer developed at SERI. The system allows the first direct ellipsometric measurement of the near infrared optical properties of low-bandgap materials such as the InGaAsP family of semiconductors. In addition, a computer program has been written which calculates, using the method of Abeles (10), the reflectance and transmittance of an n-layer stack of planar materials at an arbitrary angle of incidence. The optical constants derived from ellipsometric measurements are used in conjunction with the computer model to calculate optimal antireflection coating thicknesses for several high-efficiency solar cells.

1.2. Fresnel Equations

The relations which govern the classical interaction of light with matter may be derived from the macroscopic Maxwell's equations (11) (Gaussian units):

$$\begin{aligned}\nabla \cdot \mathbf{D} &= 4\pi\rho \\ \nabla \times \mathbf{H} - \frac{1}{c} \frac{\partial \mathbf{D}}{\partial t} &= \frac{4\pi}{c} \mathbf{J} \\ \nabla \times \mathbf{E} + \frac{1}{c} \frac{\partial \mathbf{B}}{\partial t} &= 0 \\ \nabla \cdot \mathbf{B} &= 0\end{aligned}$$

with

$$\begin{aligned}\mathbf{D} &= \mathbf{E} + 4\pi\mathbf{P} \\ \mathbf{H} &= \mathbf{B} - 4\pi\mathbf{M}\end{aligned}$$

In this system of units, the free space dielectric constant (electric permittivity) and magnetic permeability are $\epsilon_0=1$ and $\mu_0=1$. **D**, ρ , **H**, **J**, **E**, **B**, **P**, **M** and **c** are defined:

D = Displacement field (statvolt cm^{-1} , or statcoul cm^{-2})

ρ = Charge density (statcoul cm^{-3})

H = Magnetic field (oersted)

J = Current density (statamp cm^{-2})

E = Electric field (statvolt cm^{-1})

B = Magnetic induction (oersted)

P = Polarization (dipole moment cm^{-3})

M = Magnetization (magnetic moment cm^{-3})

c = Speed of light in vacuum ($2.9979\text{E}+10 \text{ cm s}^{-1}$)

Applications of Gauss' law:

$$\oint_{\text{S}} \mathbf{E} \cdot \hat{\mathbf{n}} \, da = 4\pi \int_{\text{V}} \rho(\mathbf{x}) d^3x$$

and Stokes' theorem:

$$\int_{\text{S}} (\nabla \times \mathbf{A}) \cdot \hat{\mathbf{n}} \, da = \oint_{\text{C}} \mathbf{A} \cdot d\mathbf{l}$$

at a dielectric interface lead to the boundary conditions for the normal and tangential components of **E**, **H**, **B** and **D**. The dynamic boundary conditions which govern electric

field reflection and transmission at an interface may then be derived for orthogonal (p and s) polarization states (12) (figure 4):

$$r_p = \frac{N_j^* \cos \Phi_i - N_i^* \cos \Phi_j}{N_j^* \cos \Phi_i + N_i^* \cos \Phi_j} \quad (1.1)$$

$$r_s = \frac{N_i^* \cos \Phi_i - N_j^* \cos \Phi_j}{N_i^* \cos \Phi_i + N_j^* \cos \Phi_j} \quad (1.2)$$

$$t_p = \frac{2N_j^* \cos \Phi_i}{N_j^* \cos \Phi_i + N_i^* \cos \Phi_j} \quad (1.3)$$

$$t_s = \frac{2N_i^* \cos \Phi_j}{N_i^* \cos \Phi_i + N_j^* \cos \Phi_j} \quad (1.4)$$

Φ_j = angle of incidence for i-jth interface

Note that at normal incidence (where $\Phi_i = \Phi_j = 0$), $r_p = r_s$ and $t_p = t_s$. Therefore, a non-normal angle of incidence is required to distinguish meaningfully between polarization states. The 'plane of incidence' is often used in the definition of relevant angles. This plane contains two vectors: the incident wavevector, \mathbf{k} , and the surface normal, \mathbf{n} (figure 4). Both the p and s directions are orthogonal to \mathbf{k} , but p lies in the plane of incidence, while s is perpendicular to the plane of incidence (8). Equations 1.1-1.4, often called the 'Fresnel equations,' form the basis for both the ellipsometric and reflectance/transmittance methods used in the determination of optical constants.

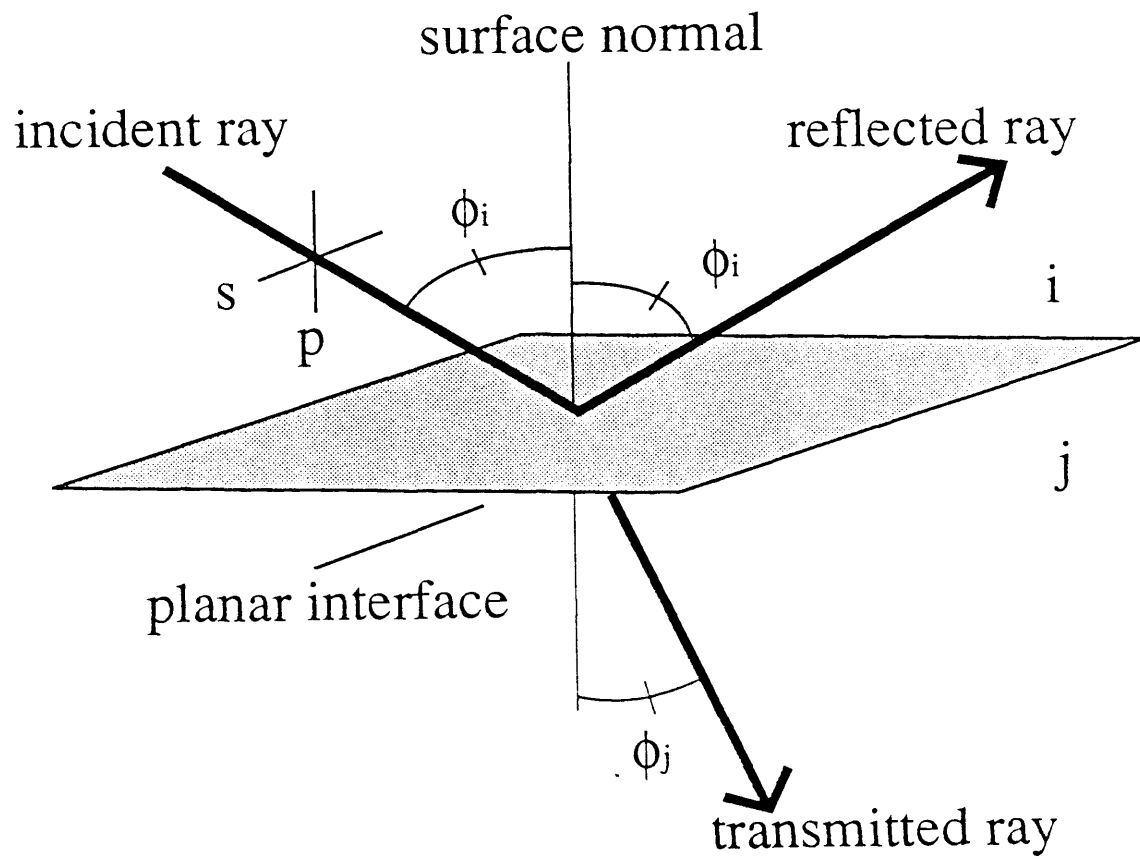


Figure 4. Illustration of the p and s polarization states, defined in relation to a planar interface.

Chapter 2

ELLIPSOMETRY

Automated scanning ellipsometry has been the method of choice for determination of $N^*(\lambda)$ in the ultraviolet (UV) and visual (VIS) regions since the mid-1970's, but near infrared (NIR) ellipsometric measurements have not been performed on even the most widely-used III-V alloys due to a lack of suitable detection systems (3). An UV-VIS-NIR (350-1700 nm) wavelength scanning ellipsometer has recently been completed at SERI. Excellent agreement has been found between SERI results and those of other laboratories for several materials (CuInSe₂, InP, etc.) throughout the UV-VIS region. NIR data are typically not available for comparison.

The basic concepts of ellipsometry are relatively simple. Linearly polarized light (generated by a light source and a linear polarizer) is reflected from a planar sample at a non-zero angle of incidence. The reflected light is, in general, elliptically polarized (8). The beam is passed through a second linear polarizer (called the "analyzer") and into some form of detection system. One polarizer is rotated, and the intensity is measured as a function of polarization angle. The intensity information is used to find the ellipticity and orientation of the reflected light, which in turn indicate (via equations 1.1-1.4) possible values of the material optical constants.

This qualitative picture is based on classical electromagnetic wave propagation and reflection. R. C. Jones and R. H. Mueller each developed mathematical constructions for the description of polarized light (12, 13). This thesis uses the Jones formalism and the conventions most commonly found in the literature for identification of the relevant angles.

The following discussion uses P and A for polarizer and analyzer angle measured with respect to the plane of incidence (figure 5).

2.1. Jones Representation of Polarized Light

The intensity of a light wave is proportional to the square of the associated electric field. This allows use of the (complex) electric field for any light propagation calculations. The Jones formulation begins with phase information intact (13):

$$\bar{\mathbf{E}} = \begin{bmatrix} E_x e^{i\Phi_x} \\ E_y e^{i\Phi_y} \end{bmatrix}$$

Propagation is in the z direction.

For linearly polarized light, the x and y components are 'in phase' ($\Phi_x = \Phi_y$). As an example, set $E_x = E_y$ and $\Phi_x = \Phi_y$ to recover a representation for linearly polarized light aligned forty five degrees from the x-axis:

$$\bar{\mathbf{E}} = E_x e^{i\Phi_x} \begin{bmatrix} 1 \\ 1 \end{bmatrix}$$

and normalize ($|\mathbf{E}|^2=1$, forcing loss of phase information):

$$\bar{\mathbf{E}} = \frac{1}{\sqrt{2}} \begin{bmatrix} 1 \\ 1 \end{bmatrix}$$

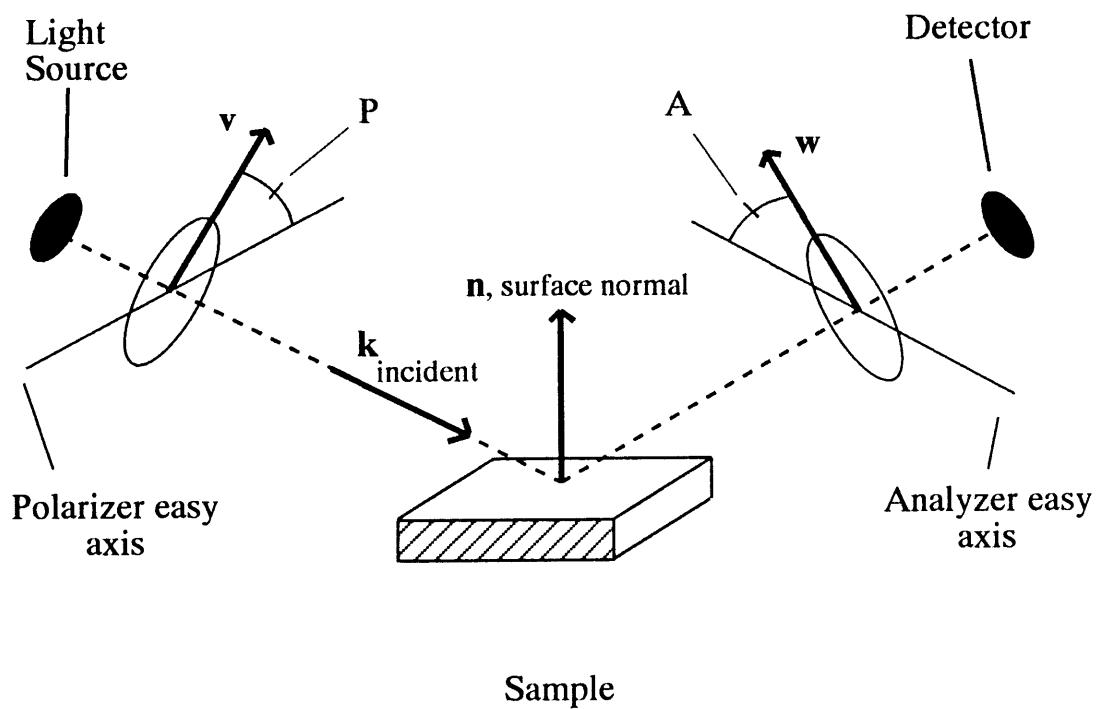


Figure 5. Illustration of the polarizer and analyzer angles, P and A . The plane containing $\mathbf{k}_{\text{incident}}$ and \mathbf{n} defines the "plane of incidence." The vectors \mathbf{v} and \mathbf{w} are in the plane of incidence, and provide references for measurement of P and A .

Similar representations may be obtained for right-circular ($\Phi_x - \Phi_y = \pi/2$), left-circular ($\Phi_x - \Phi_y = -\pi/2$) or general elliptic ($E_x \neq E_y$) polarization states (13).

2.2. Basic Equations of Ellipsometry

The electric field at the ellipsometer detector may be derived using a series of coordinate rotations and the Jones formalism (13). The standard 2x2 matrix rotation from system 'a' to system 'b' is:

$$R(\gamma) = \begin{bmatrix} \cos \gamma & -\sin \gamma \\ \sin \gamma & \cos \gamma \end{bmatrix}$$

where γ is the angle between the x-axis in system 'a' and the x-axis in system 'b.' The following derivation is for the rotating polarizer, fixed analyzer configuration, although the mathematics is essentially the same for the case of a rotating analyzer, fixed polarizer.

The Jones matrices for reflection from a surface and transmission through a linear polarizer are quite simple when expressed in the local coordinate system of the sample or polarizer (see, e.g., the "sample" and "T" matrices, below). The coordinate systems of the polarizer and analyzer are, in general, aligned at arbitrary angles P and A with respect to the plane of incidence (figure 5). A derivation of the light intensity at the ellipsometer detector is simplified if propagation of the polarized beam is described with a series of local

coordinate rotations between optic elements. The calculation is performed using matrix multiplication (right-to-left) in the following manner (13):

$$[E_{\text{detector}}] = [R(A)][T][R(-A)][\text{Sample}][R(P)][E_o]$$

where:

$$[E_o] = \begin{bmatrix} 1 \\ 0 \end{bmatrix} \quad \text{Linearly polarized light from rotating polarizer}$$

$$[R(P)] = \begin{bmatrix} \cos(P) & -\sin(P) \\ \sin(P) & \cos(P) \end{bmatrix} \quad \text{Rotation to sample's frame of reference}$$

$$[\text{Sample}] = \begin{bmatrix} r_p & 0 \\ 0 & r_s \end{bmatrix} \quad \text{Sample reflection (with Fresnel coefficients)}$$

$$[R(-A)] = \begin{bmatrix} \cos(A) & \sin(A) \\ -\sin(A) & \cos(A) \end{bmatrix} \quad \text{Rotation to analyzer's frame of reference}$$

$$[T] = \begin{bmatrix} 1 & 0 \\ 0 & 0 \end{bmatrix} \quad \text{Transmission along analyzer axis}$$

$$[R(A)] = \begin{bmatrix} \cos(A) & -\sin(A) \\ \sin(A) & \cos(A) \end{bmatrix} \quad \text{Rotation to sample's frame of reference}$$

The intensity at the detector ($\propto |E_{\text{detector}}|^2$) is independent of the final axis rotation, $R(A)$. Thus, carrying out the multiplication:

$$\begin{aligned}
I_{\text{detector}} &\propto \left[\begin{array}{c} r_p \cos(P) \cos(A) + r_s \sin(P) \sin(A) \\ 0 \end{array} \right]^2 \\
&\propto \{r_p^* \cos(P) \cos(A) + r_s^* \sin(P) \sin(A)\} \times \\
&\quad \{r_p \cos(P) \cos(A) + r_s \sin(P) \sin(A)\} \\
&\propto |r_p|^2 \cos^2(A) + |r_s|^2 \sin^2(A) + \{|r_p|^2 \cos^2(A) - |r_s|^2 \sin^2(A)\} \cos(2P) \\
&\quad + 2 \operatorname{Re}(r_p r_s^*) \sin(A) \cos(A) \sin(2P)
\end{aligned}$$

Rearrange terms and normalize so that the average intensity equals 'c':

$$\begin{aligned}
I_{\text{detector}} &= c + c \times \cos(2P) \times \frac{|r_p|^2 \cos^2(A) - |r_s|^2 \sin^2(A)}{|r_p|^2 \cos^2(A) + |r_s|^2 \sin^2(A)} \\
&\quad + 2c \times \sin(2P) \times \frac{2 \operatorname{Re}(r_p r_s^*) \sin(A) \cos(A)}{|r_p|^2 \cos^2(A) + |r_s|^2 \sin^2(A)} \\
&= c + c \left(\frac{\left(\frac{|r_p|^2}{|r_s|^2} - \tan^2(A) \right)}{\left(\frac{|r_p|^2}{|r_s|^2} + \tan^2(A) \right)} \right) \cos(2P) + 2c \left(\frac{\operatorname{Re} \left(\frac{r_p}{r_s} \right) \tan(A)}{\left(\frac{|r_p|^2}{|r_s|^2} + \tan^2(P) \right)} \right) \sin(2P)
\end{aligned}$$

The 'ellipsometric equation' may be used to define quantities Ψ and Δ (8, 12, 13):

$$\frac{r_p}{r_s} = \tan \Psi e^{i\Delta} \tag{1.5}$$

so that

$$\left| \frac{r_p}{r_s} \right|^2 = \tan^2 \Psi$$

and

$$\operatorname{Re} \left(\frac{r_p}{r_s} \right) = \tan \Psi \cos \Delta$$

where r_p and r_s are the electric field reflection coefficients for p and s polarizations defined in equations 1.1-1.4. Upon substitution, the expression for intensity becomes:

$$I_{\text{detector}} = c + c \left(\frac{\tan^2 \Psi - \tan^2 A}{\tan^2 \Psi + \tan^2 A} \right) \cos(2P) + 2c \left(\frac{\tan \Psi \cos \Delta \tan A}{\tan^2 \Psi + \tan^2 A} \right) \sin(2P)$$

Now put

$$a = c \left(\frac{\tan^2 \Psi - \tan^2 A}{\tan^2 \Psi + \tan^2 A} \right) \quad \text{and} \quad b = 2c \left(\frac{\tan \Psi \cos \Delta \tan A}{\tan^2 \Psi + \tan^2 A} \right) \quad (1.6)$$

so that the intensity variation may be simply expressed in terms of the three measurable Fourier coefficients, a, b and c:

$$I_{\text{detector}} = c + a \cos(2P) + b \sin(2P) \quad (1.7)$$

The ellipsometer measures I_{detector} as a function of polarizer angle, and least squares Fourier series analysis is implemented to solve for a, b and c. Finally, equations 1.6 may be inverted to gain expressions for $\tan(\Psi)$ and $\cos(\Delta)$ as functions of the Fourier coefficients and analyzer angle:

$$\tan \Psi = \sqrt{\frac{c+a}{c-a}} \tan A \quad (1.7)$$

$$\cos \Delta = \pm \frac{b}{\sqrt{c^2 - a^2}} \quad (1.8)$$

The values of Ψ and Δ , which have now been determined explicitly, in conjunction with the ellipsometric equation (1.5), are used to solve for r_p/r_s for the pre-set value of the angle of incidence. Since r_p/r_s is determined by the optical constants of the material under study, via the Fresnel equations (1.1-1.4), measurement of Ψ and Δ allows solution for N^* at each wavelength.

2.3. The SERI UV-VIS-NIR Scanning Ellipsometer

2.3.1. Ellipsometer Configuration

The SERI scanning ellipsometer is designed for use in the rotating polarizer, fixed analyzer (RPA) configuration (figure 6). This type of ellipsometer exhibits low sensitivity to room light (since the detector gathers light which passes through a high f-number

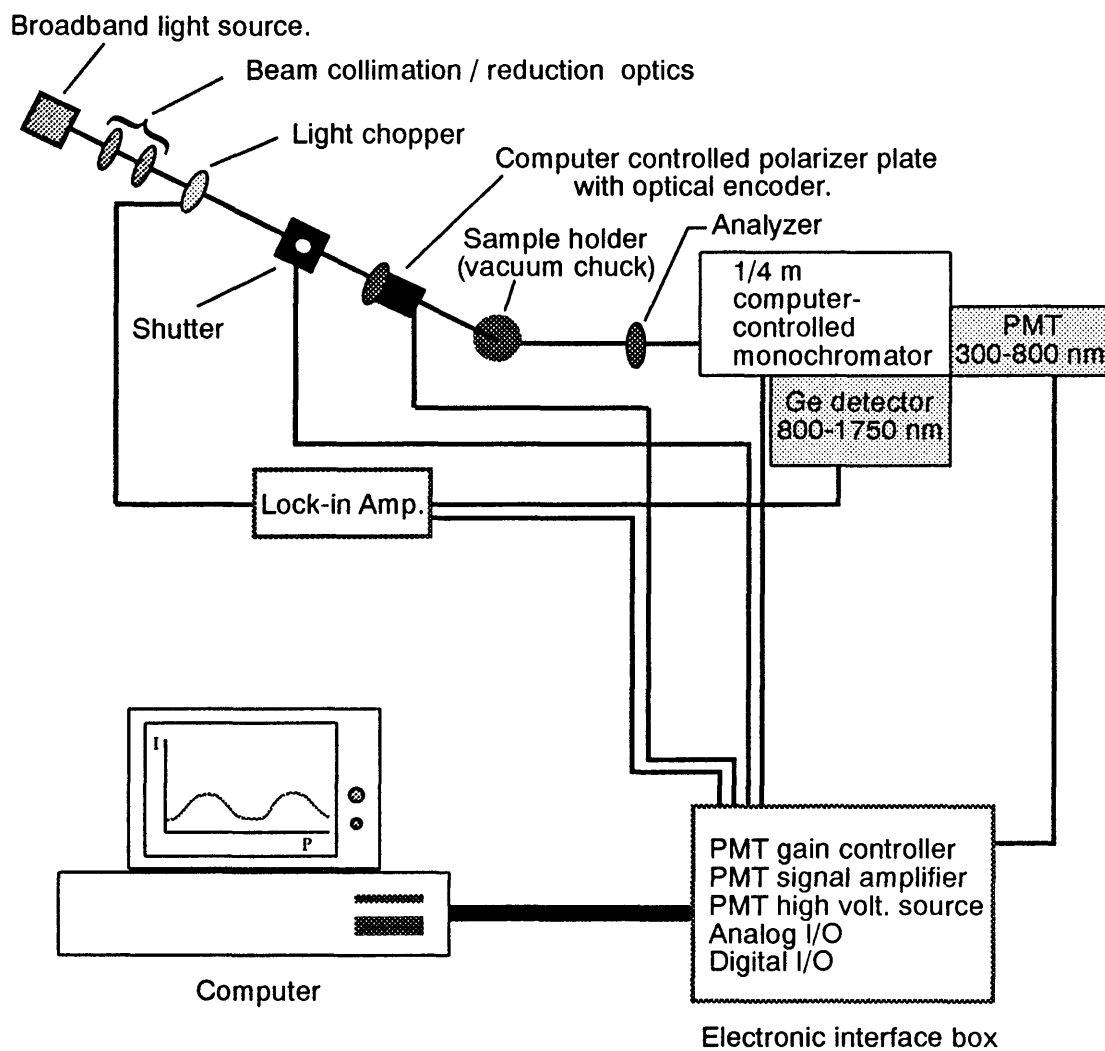


Figure 6. Wavelength scanning ellipsometer. Operating range: 350-1700 nm.

monochromator), but it is sensitive to light source polarization. Some systems use additional 'depolarizing' optics at the light source output to minimize this effect, but reflective and diffuse power losses are associated with the addition of optical components. Therefore, a simple method has been devised in which the partial polarization is measured, and correction coefficients are applied during the real-time acquisition of Ψ and Δ , as described below.

An experimentally verified polarization-insensitive end-on photomultiplier tube is used to measure the intensity as a function of polarizer angle of light incident upon the sample. Interference filters are used to produce nearly monochromatic light at the detector. The transmittance of these filters is shown in figure 7. Fourier analysis of the ellipsometer intensity curve yields partial polarization coefficients. These are normalized (i.e.- set $c=1$, figure 8), and their inverse values are used as multiplicative correction factors to the measured Fourier coefficients (a, b and c, described previously). This technique also removes effects which are not necessarily caused by source polarization. For instance, slightly misaligned polarizers cause small beam 'wobbles' (periodic with the polarizer rotation) which are normalized with this process.

2.3.2. Monochromator

A single-grating 1/4-meter monochromator is used over the wavelength range 350-1700 nm. Gratings blazed at 250, 500 and 1000 nm may be substituted during a measurement to maintain optimal signal throughput. The full-width-half-maximum (FWHM) wavelength resolution is 3.4 nm with 0.60 mm input and exit slits, as measured

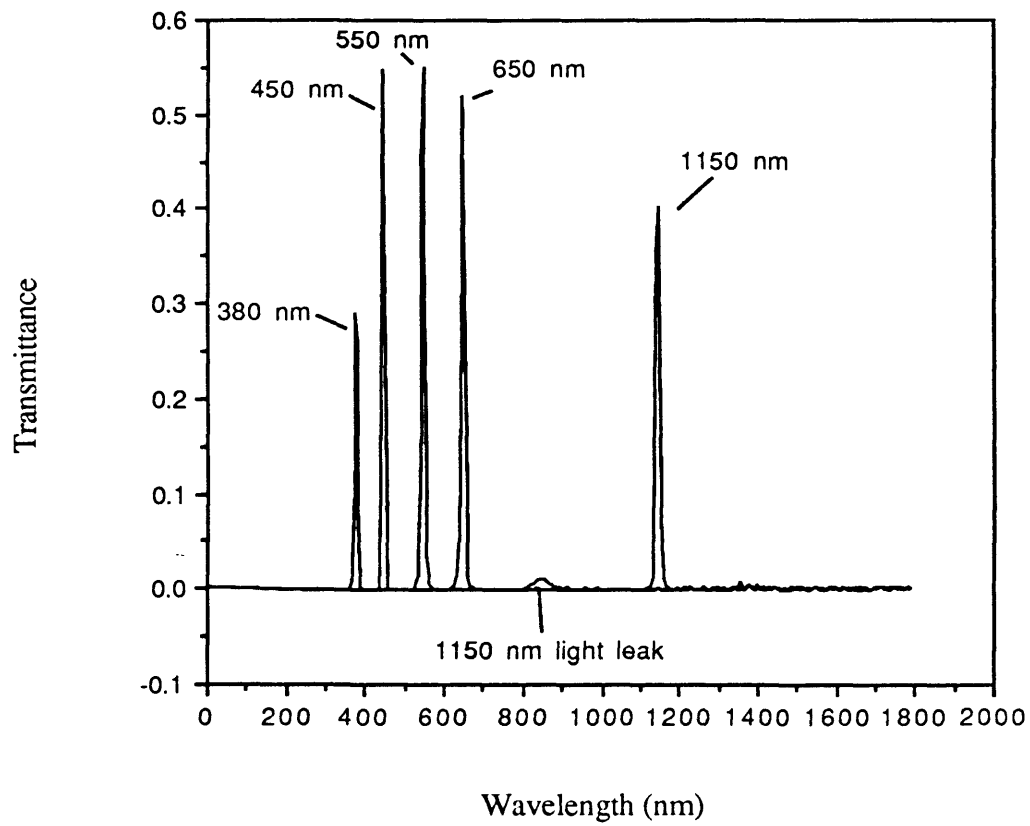


Figure 7. Transmittance curves for the single-wavelength interference filters used in the calibration of the ellipsometer light source partial polarization coefficients.

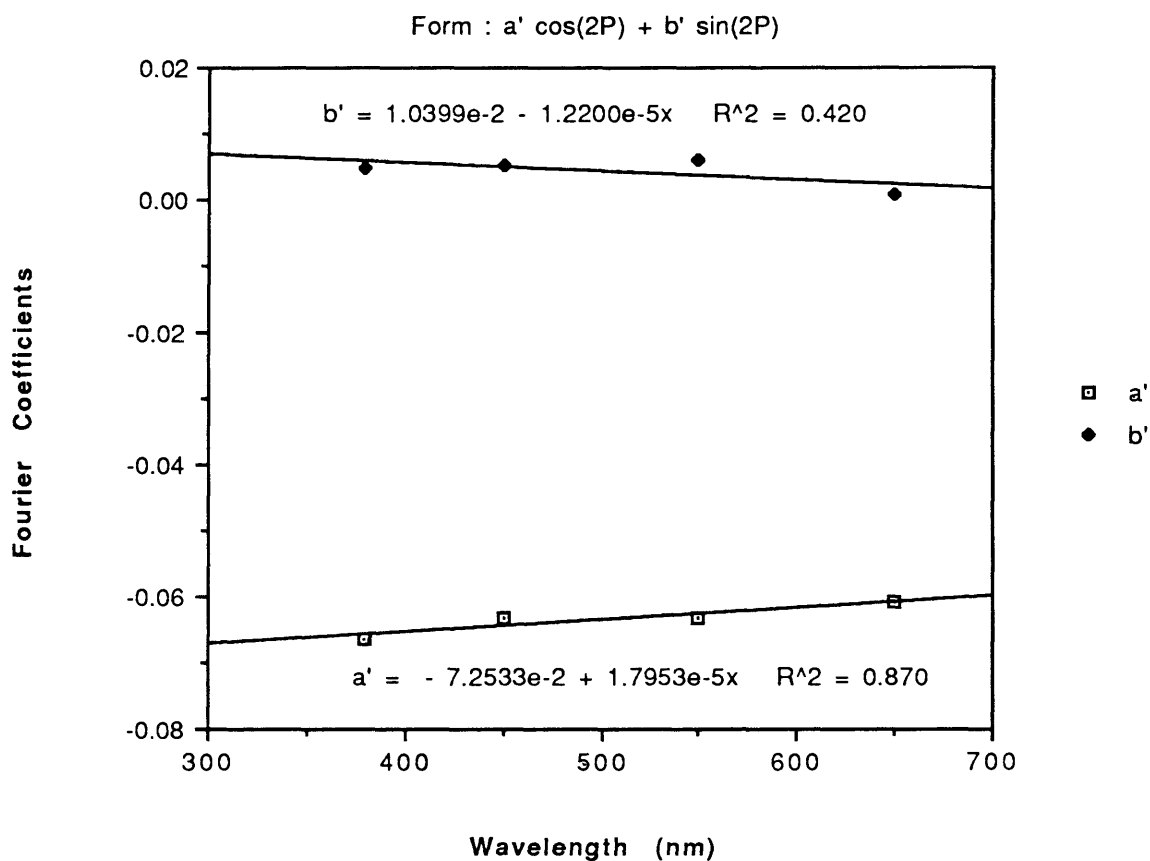


Figure 8. Normalized Fourier coefficients used in the calibration of the partial polarization of the light source.

at the helium-neon (632.8 nm) wavelength. Wavelength offsets have been determined with a mercury calibration lamp, and the corrections are applied automatically.

A simple monochromator suffers from two major drawbacks which may affect the ellipsometric results. First, if the monochromator is set at a wavelength λ , then higher orders (λ/n , $n=2,3,4,\dots$) are also passed to the detector. Specific filters must be used in each wavelength range to remove higher order signals. Figure 9 shows transmittance curves of the five order-sorting filters used in the ellipsometer. These color-glass filters are placed close to the light-source output, and hence their transmittances must be measured periodically to check for unwanted degradation or leakage.

Stray light of any wavelength is also passed through a monochromator. The intensity is usually quite small, and for reasonable experimental signals the stray light contribution is negligible. It is essential, however, to remain in wavelength regions where the signal to noise ratio is high. Low signals (light intensities) require high detector gain, thus allowing significant stray light contribution to the measured intensity.

2.3.3. Detectors

A gallium arsenide end-on photomultiplier tube (PMT) is used in the wavelength range 350-800 nm. High quality polarizers (discussed later) will allow the range to be extended much farther into the UV. The PMT gain is computer controlled through standard input/output digital to analog converters (DACs). A 12-bit, 0-10 volt analog to digital converter (ADC) returns the PMT output voltage to the computer. At each wavelength, the polarizer is repeatedly swept through full rotations while the PMT output is monitored.

Wheel Position #	Oriel Catalog #	Schott Catalog #	Minimum λ nm/T	Maximum λ nm/T
1	51650	UG5	225/0.25	300/0.92
2	51225	WG295	300/0.90	425/1.00
3	51272	GG400	425/0.90	740/1.00
4	51340	RG695	740/0.90	1300/0.9
5	51362	RG1000	1300/0.8	1700/0.8

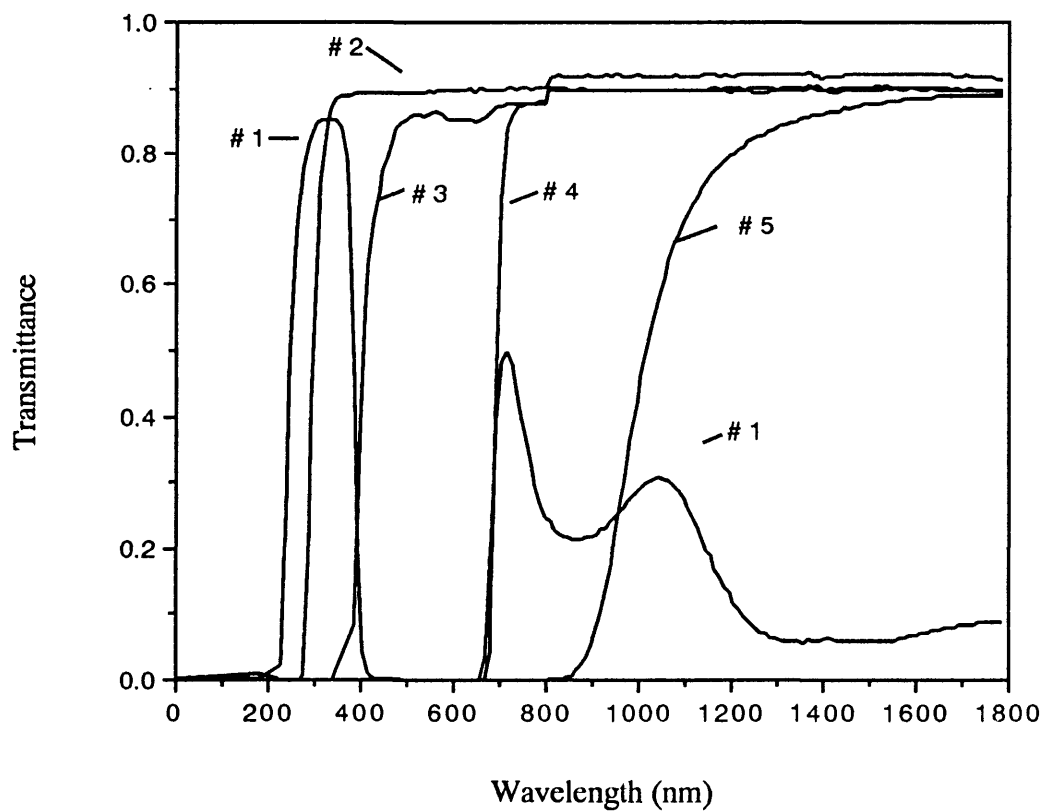


Figure 9. Transmittance curves of the ellipsometer order sorting filters as measured by a CARY 2300 spectrophotometer. A table of the manufacturer's specifications is included.

The PMT gain is adjusted until the maximum output lies between 8.5 and 9.5 volts. This effectively takes advantage of the full ADC input voltage range, thus minimizing digitization effects (digitization is approximately 0.03% of the full-scale signal). The time required for the PMT optimization process is usually less than one second.

The background and dark current contributions to the detector signal can be significant, even in the RPA configuration. When the PMT is in use (350-800 nm wavelength range), an extra polarizer rotation with the light source shuttered is necessary for ambient signal removal. This function may be defeated if higher scan rates are required, but room lights should be turned off in this mode.

In the NIR (800-1700 nm), light-chopping and lock-in techniques are employed in conjunction with a liquid nitrogen cooled germanium detector. This is the first time that this combination has been successfully implemented for NIR ellipsometric measurements. Only one polarizer rotation is necessary at each wavelength, since the lock-in electronically removes ambient and noise contributions from the detector DC output line. As in the case of the PMT, a software algorithm optimizes the detector output at each wavelength before initiating the measurement. The major difference is that the germanium detector is a fixed-gain device: therefore, the signal amplification control is implemented with the lock-in sensitivity settings. IEEE-488 communications are used to control the lock-in settings, and the DC output is hardwired to an ADC for high-speed (12kHz) signal averaging.

2.3.4 Light Source

The SERI ellipsometer uses a 150 watt quartz-tungsten-halogen (QTH) light source. The QTH lamp was chosen for its smooth spectral output, high stability and strong NIR emissivity. A xenon lamp should be used if higher energy (200-360 nm) optical structure is to be resolved, although care must be taken regarding the lamp's production of excessive amounts of ozone.

One drawback of the QTH lamp is that it is an 'extended' source. That is, the filament size is larger than the desired beam width. It is also difficult to achieve a uniform beam intensity distribution, since the filament exhibits a decidedly non-uniform radiation pattern. This system uses a minimum number of beam collimation lenses and several small apertures to reduce the beam to the desired size and divergence. Much of the original light is wasted, since only one portion of the filament is focussed. The result, however, is a spatially uniform output beam.

2.3.5. Polarizer and Analyzer

The polarizer is an air-spaced calcite (Glan-Foucault) design (figure 10a), which eliminates the o-ray through total internal reflection and passes the e-ray with minimal beam deviation (13). Calcite polarizers exhibit high transmittance from 230-5000 nm, while quartz or magnesium fluoride (MgF_2) polarizers may be used at shorter wavelengths (180 and 130 nm, respectively). The quartz and MgF_2 polarizers, however, are available only in the Rochon configuration (figure 10b). The Rochon polarizer separates

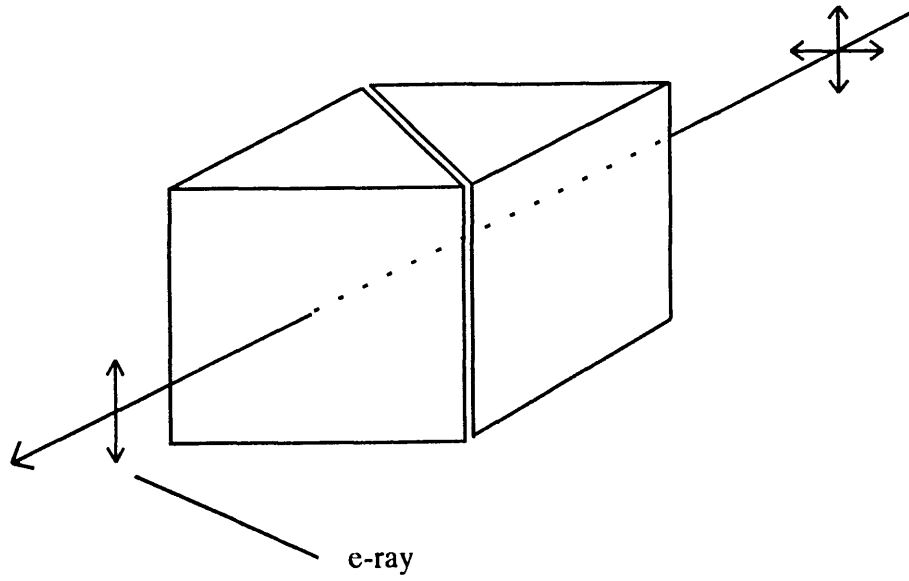


Figure 10a. The Glan-Foucault polarizing prism. One linearly polarized beam exits the

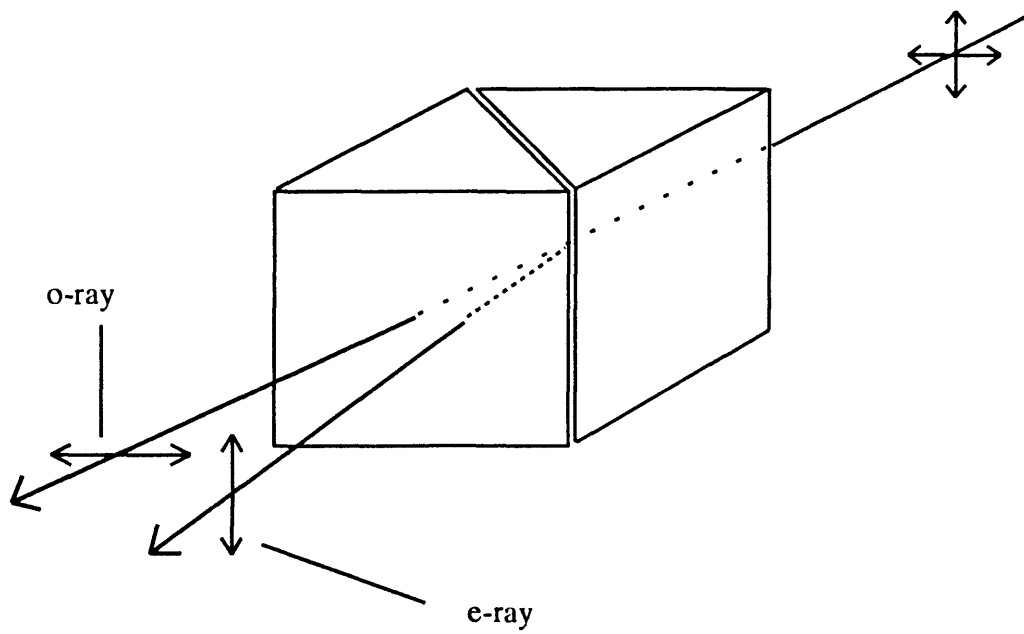


Figure 10b. The Rochon polarizer configuration. Both the o- and e-rays are passed through the crystal.

the o and e-rays by only a few degrees in the ultraviolet, and the angle decreases at longer wavelengths (13). This property makes the Rochon configuration unsuitable for NIR ellipsometry, since the rays must be completely separable at the detector.

The stepper motor which controls the polarizer position is computer-controlled via an RS-232 serial interface. It utilizes a 'smart' controller with on-board RAM and EEPROM's. Position sequences may be downloaded to the controller, and velocity and acceleration profiles are completely controllable with a resolution of 12800 steps/rotation. All movements are referenced to an arbitrary 'home' position, and an external optical encoder (emitter/detector diode pair) is used to ensure that this position remains stable to within 0.029 degrees. The analyzer crystal is identical to the polarizer, but no computer controlled positioning is implemented.

2.3.6. Computer Control

Input and output is controlled by an 80386-based computer. The interface software (written in the Pascal programming language) implements menus and other user-friendly objects to minimize the learning time. Determination of Ψ and Δ at only one wavelength typically requires fifteen to thirty seconds and may involve the acquisition, averaging and Fourier series analysis of up to 40,000 data points. The Ψ , Δ information is stored to disk for later reduction with the appropriate physical model (substrate only, substrate plus oxide, etc.). The final conversion from Ψ and Δ to N and k for the more complicated

multi-layer systems is performed by software from the Applied Software Engineering Company.

2.4. Ellipsometric Results

Ellipsometry is primarily a probe of surface optical properties for sufficiently absorptive materials. The presence of thin oxide layers or surface roughness is the largest obstacle in the determination of true 'bulk' indices of refraction. There are two general approaches to the surface quality problem: 1) elimination of pre-existing native oxides and surface roughness with appropriate chemo-mechanical treatment (14) and 2) incorporation of these layers in the final data analysis process (15). Each method poses a unique set of problems to the researcher.

This thesis employs a new variant of method 1), above. A lattice-matched capping material is retained on the sample until just prior to an ellipsometric scan. The material is selectively removed and the measurement proceeds in a nitrogen and argon atmosphere to inhibit oxide growth. Argon, which is denser than air, is 'dropped' past the surface of the sample with an inverted polyethylene (acid resistant) cup. Liquid nitrogen boil-off gas is available for additional air displacement, if desired.

The selective etchants which were used in this study are shown in the table below. The rates for $\text{In}_{0.25}\text{Ga}_{0.75}\text{As}_{0.54}\text{P}_{0.46}$ are similar to those for $\text{In}_{0.53}\text{Ga}_{0.47}\text{As}$. Etch rates for 23°C $10\text{H}_2\text{SO}_4:1\text{H}_2\text{O}_2:1\text{H}_2\text{O}$ and $2\text{NH}_4\text{OH}:1\text{H}_2\text{O}_2:2\text{H}_2\text{O}$ were determined soon after mixing, and thus represent the maximum room temperature etch rate for the indicated

mixture. All rates were determined by a combination of profilometry and selective masking techniques.

Etchants and etch rates ($\pm 10\%$, unless otherwise indicated) for the materials InP and $\text{In}_{0.53}\text{Ga}_{0.47}\text{As}$.

	InP	$\text{In}_{0.53}\text{Ga}_{0.47}\text{As}$
HCl	$8 \mu\text{m}/\text{minute}$	$250 \text{ \AA}/\text{minute}$
$10 \text{ H}_2\text{SO}_4 : 1 \text{ H}_2\text{O}_2 : 1 \text{ H}_2\text{O}$	$100 \text{ \AA}/\text{minute}$	$0.8 \mu\text{m}/\text{minute}$
$2 \text{ NH}_4\text{OH} : 1 \text{ H}_2\text{O}_2 : 2 \text{ H}_2\text{O}$	$13 \text{ \AA}/\text{minute} (\pm 20\%)$	$0.18 \mu\text{m}/\text{minute}$

2.4.1. Indium Phosphide

The wavelength scanning ellipsometer results for InP (nominally undoped) are shown in figure 11. No capping material was available for this sample, so a more typical chemical pretreatment scheme (14) was employed just prior to measurement. Due to the selective etch nature of $10\text{H}_2\text{SO}_4:1\text{H}_2\text{O}_2:1\text{H}_2\text{O}$, InGaAs would be a good choice for an InP capping material. Trichloroethylene, acetone and isopropyl alcohol rinses were used to remove organics and degrease the sample surface. A 1 vol. % bromine:methanol ('1% BrMeOH') etchant was then sprayed for 15 seconds to help remove the surface oxide, followed by a 0.01% BrMeOH polishing step, and finally a methanol rinse.

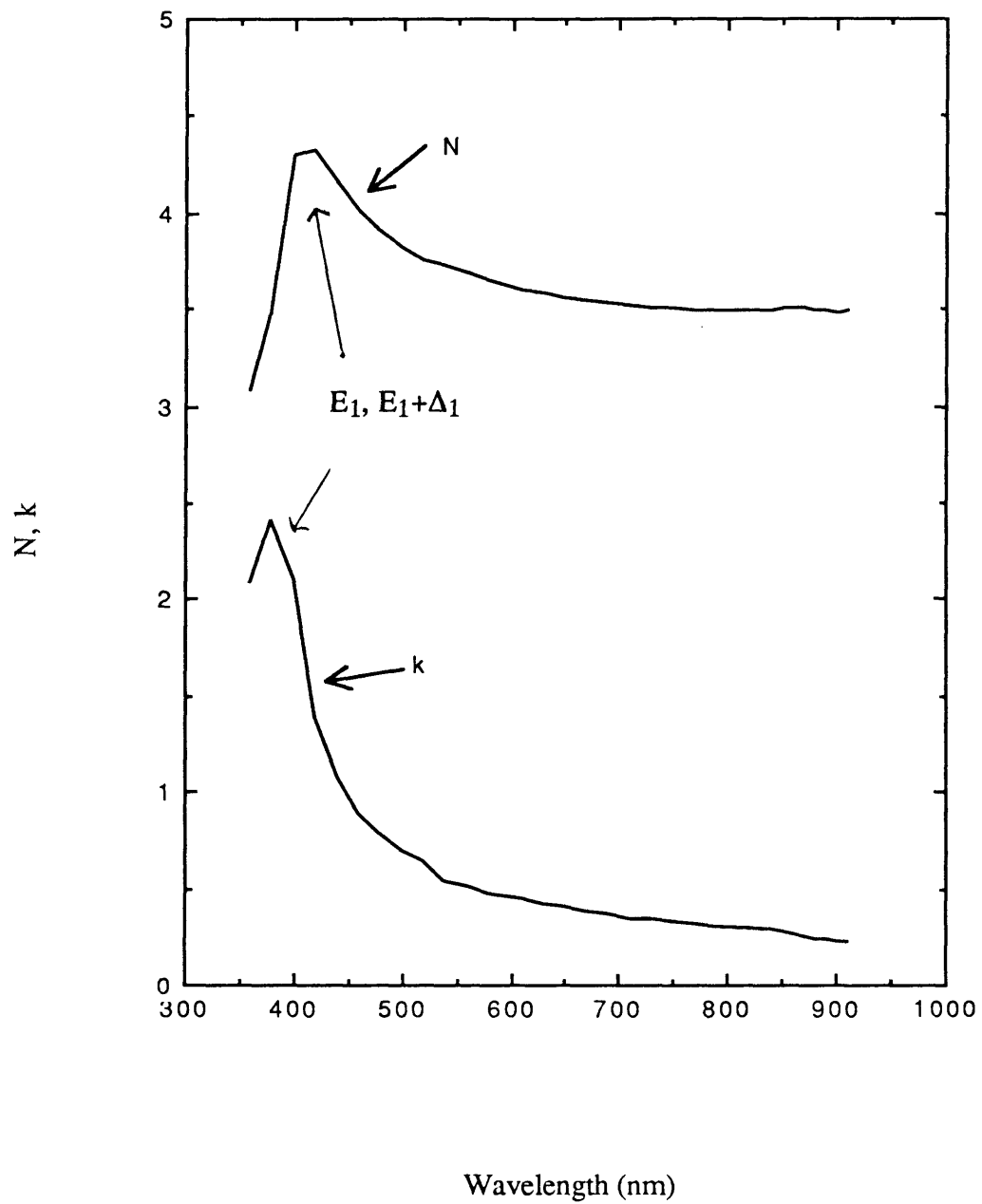


Figure 11. Ellipsometrically determined N and k of nominally undoped InP. The angle of incidence was 70° .

The sample was then immersed in the argon gas stream, and the measurement proceeded. The ellipsometric data of Aspnes and Studna and the reflectance/transmittance data of Pettit and Turner (all from reference 16) are superimposed on the SERI results in figure 12. Differences in the k-values are most likely due to the differences in sample dopant levels and surface treatments.

2.4.2. Indium Gallium Arsenide

Results for organo-metallic vapor phase epitaxy (OMVPE) grown $\text{In}_{0.53}\text{Ga}_{0.47}\text{As}$ (p-type, $p \sim 1 \times 10^{18} \text{ cm}^{-3}$) are shown in figure 13. The sample had a $\sim 1 \mu\text{m}$ lattice-matched InP cap which was removed with concentrated hydrochloric acid just prior to the measurement. The argon air-displacement technique described earlier allows some mixing with the ambient, and it only slows oxide growth, rather than preventing it completely. This run graphically demonstrates the effect of a surface oxide and/or organics. The data at wavelengths longer than 690 nm were acquired soon after the hydrochloric etch, while the data below 690 nm were collected after a three hour delay. The change in N at 690 nm is approximately 2%, while k changed by nearly 17%. This is a reasonable estimate of the percentage change in the measured dielectric function (in the visible part of the spectrum) due to the presence of thin ($< 20 \text{ \AA}$) surface oxides and contaminants. Other studies have found similar changes in N and k ($\sim 3\%$ and $\sim 20\%$, respectively) due to the presence of a 10 angstrom oxide layer (17).

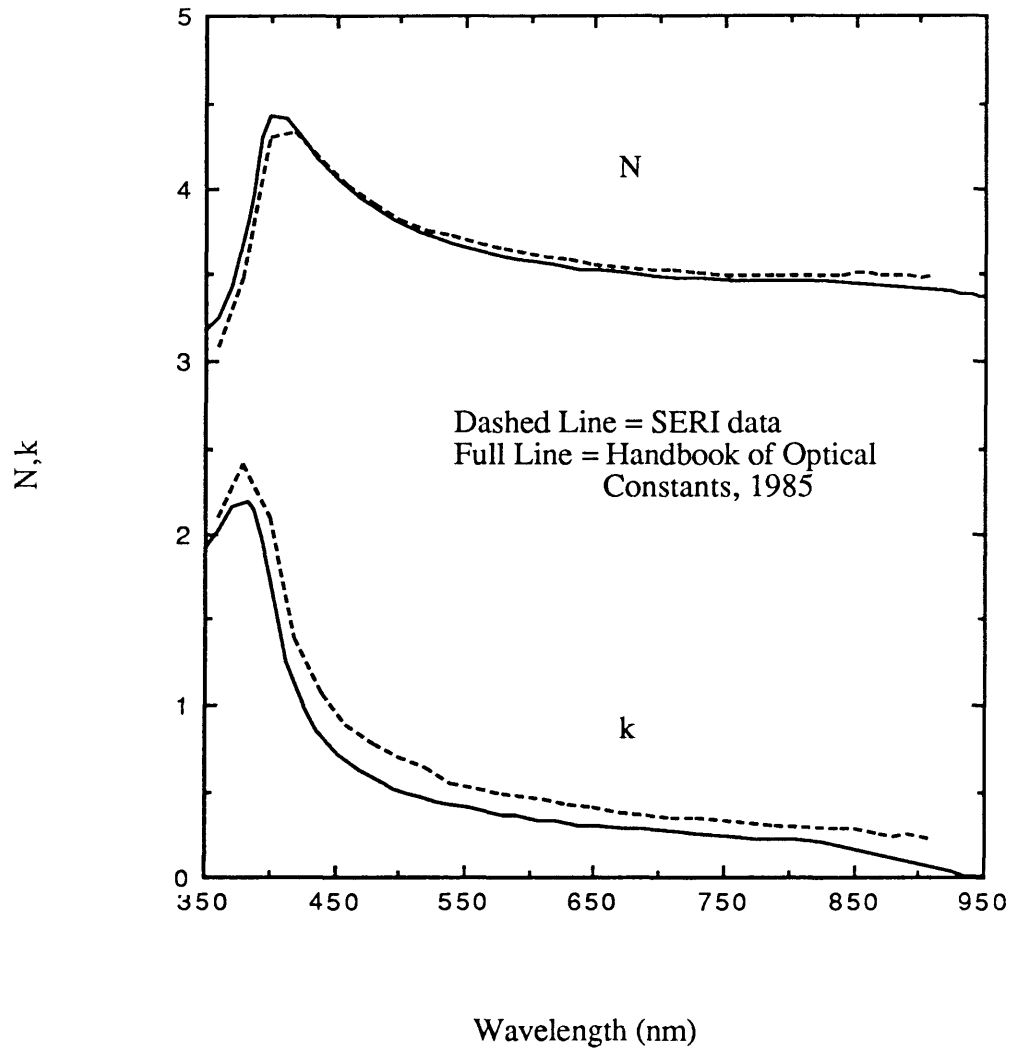


Figure 12. Comparison of InP N,k data with that of Aspnes and Studna and Pettit and Turner (16).

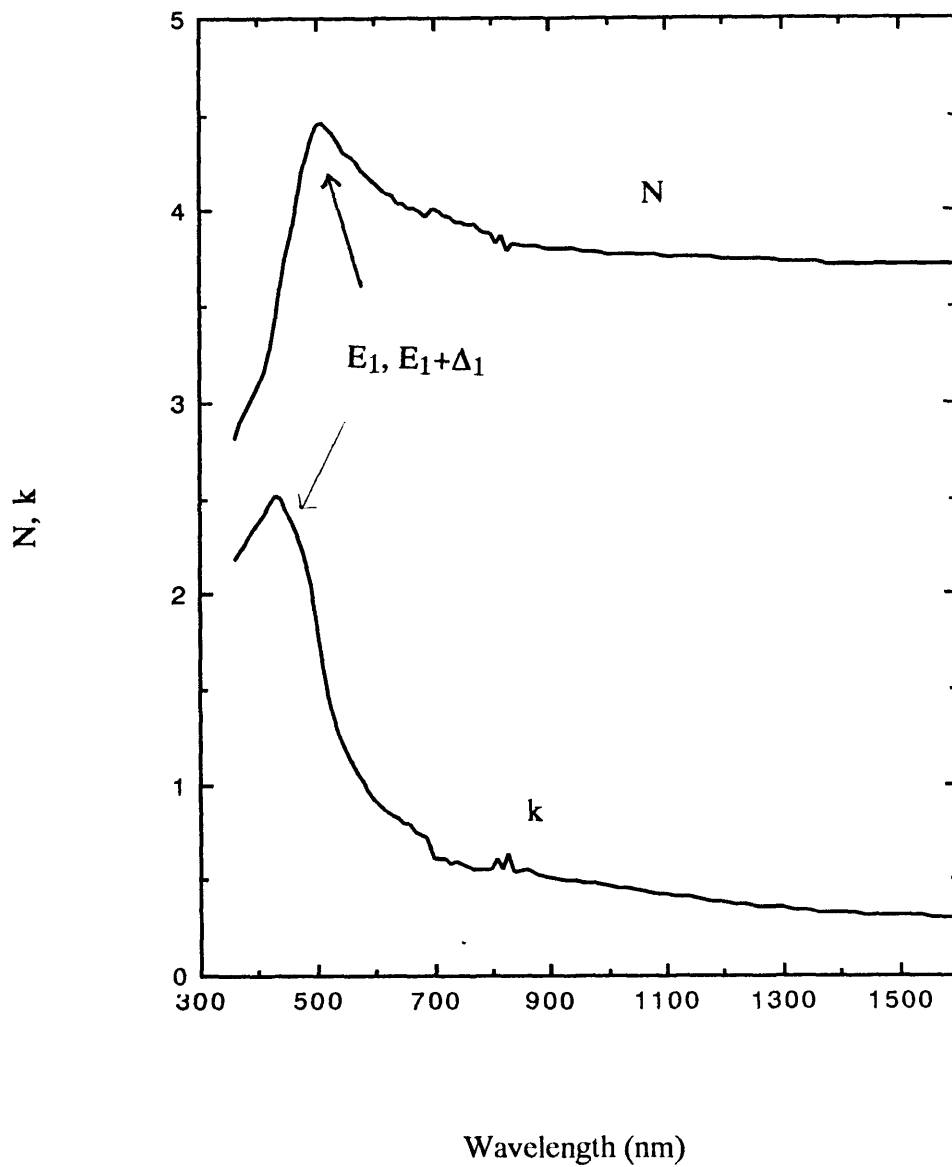


Figure 13. N and k of p-type ($p \sim 1 \times 10^{18} \text{ cm}^{-3}$) $\text{In}_{0.53}\text{Ga}_{0.47}\text{As}$ (angle of incidence = 70°). The data at wavelengths less than 690 nm were acquired after the unintentional growth of a surface oxide.

2.4.3. Indium Gallium Arsenide Phosphide

Figure 14 shows an ideal run with the quaternary $\text{In}_{0.25}\text{Ga}_{0.75}\text{As}_{0.54}\text{P}_{0.46}$ (n-type, $n \sim 1 \times 10^{18} \text{ cm}^{-3}$). A $\sim 0.1 \mu\text{m}$ thick lattice-matched InP cap was removed just prior to the measurement. There is no evidence of the detector change at 800 nm, indicating that the ellipsometer optical components are optimally aligned. An entire run takes approximately 100 minutes, during which time surface oxides may grow. To minimize the effect on the data, the scan always ends at longer wavelengths where surface oxides least affect the results.

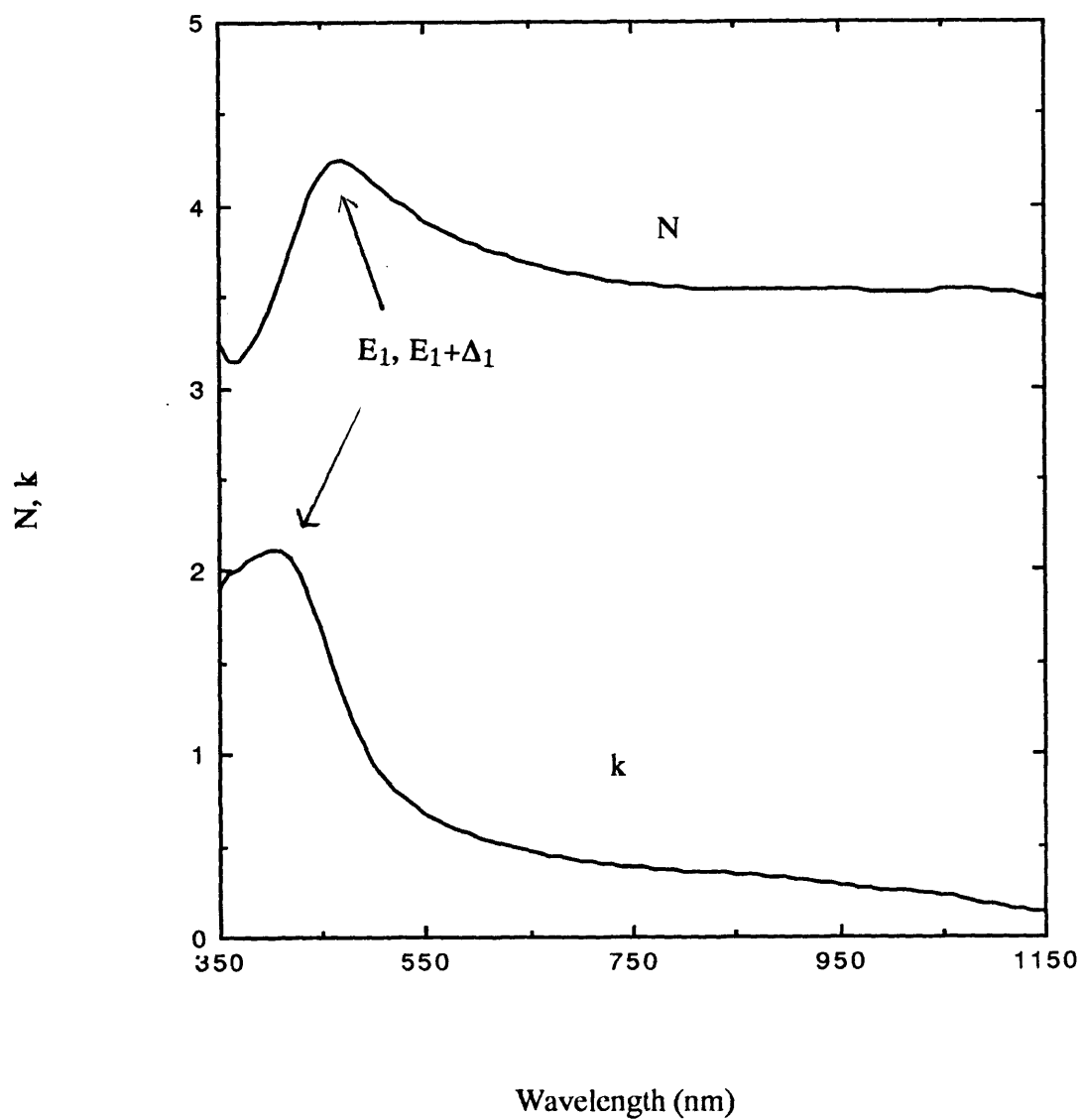


Figure 14. N and k of n-type ($n \sim 1 \times 10^{18} \text{ cm}^{-3}$) $\text{In}_{0.25}\text{Ga}_{0.75}\text{As}_{0.54}\text{P}_{0.46}$ (angle of incidence = 75°).

Chapter 3

REFLECTANCE/ TRANSMITTANCE

A CARY 2300 UV-VIS-NIR spectrophotometer has been interfaced to a Macintosh Iix for computerized acquisition of reflectance and transmittance data. When required, automatic correction may be made for variations in the 0% and 100% reflectance or transmittance references. The instrument may be operated in several modes, including specular and diffuse transmittance and reflectance. A barium sulphate-coated integrating sphere is used during diffuse component measurements, and reflectance standards are regularly measured to provide real-time normalization of the data.

All of the materials in this study become nearly transparent at some wavelength in the near infrared. This allows measurement of two parameters, reflectance (R) and transmittance (T), at sub-bandgap energies. The real and imaginary parts of the index of refraction may be calculated from R and T data for specific sample geometries.

In general, R and T may be written as functions of the layer thicknesses and indices of refraction (18). A computerized search routine is employed which varies N^* of the unknown layer until experimental R and T match calculated R and T. The process is repeated at prescribed wavelength intervals to generate $N^*(\lambda)$. The software currently in use was developed for SERI by a sub-contractor.

A sample of $\text{In}_{0.53}\text{Ga}_{0.47}\text{As}$ of suitable geometry and substrate doping level was used to calculate $N^*(\lambda)$ over a limited wavelength range near the bandgap. These data are compared with the ellipsometric results in figure 15. The R/T results suffer from inherent exponential sensitivity to the thickness of the sample (see section 4.2.2,

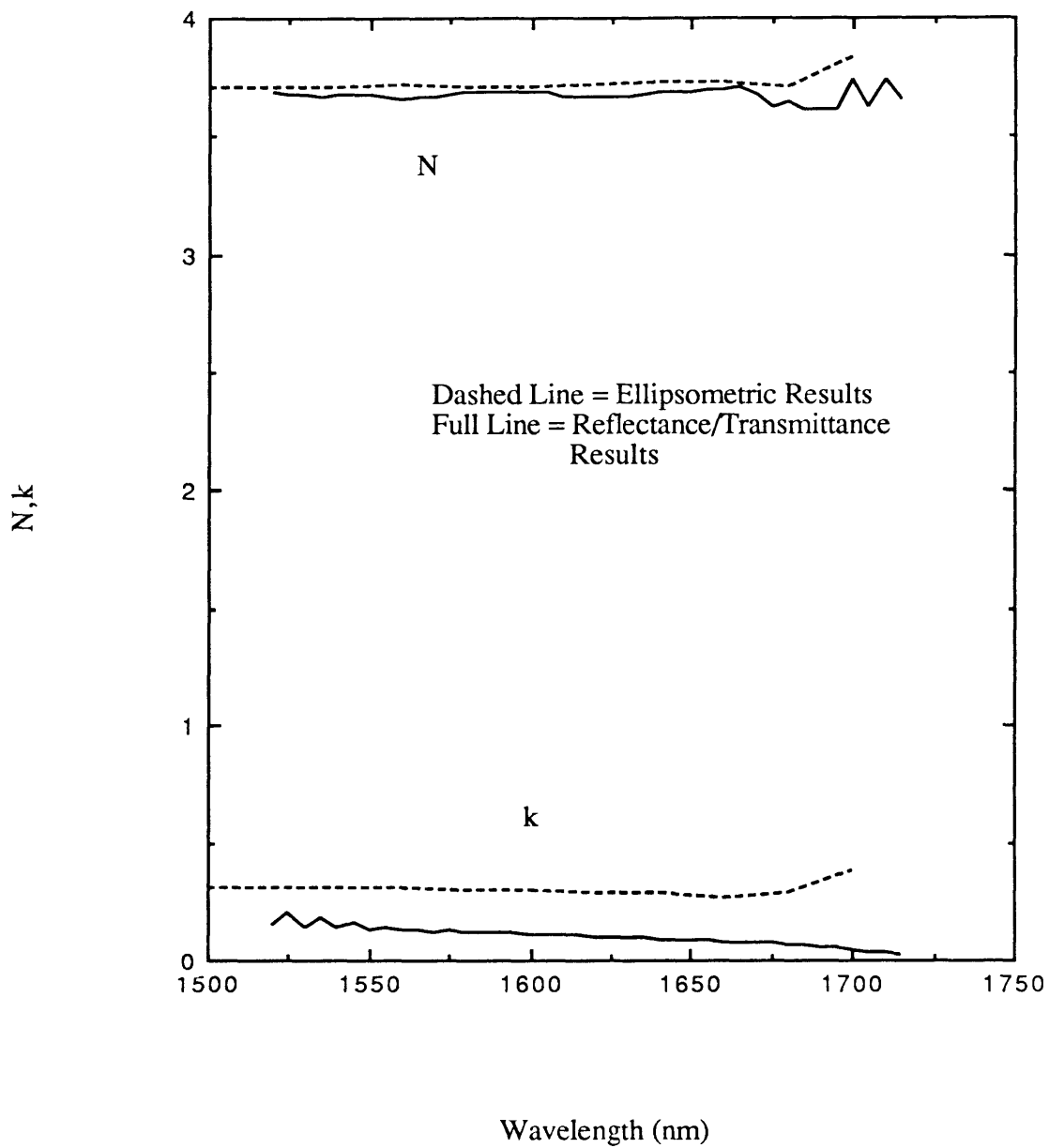


Figure 15. Comparison of N and k of $\text{In}_{0.53}\text{Ga}_{0.47}\text{As}$ as determined by ellipsometry and reflectance/transmittance. Basic ellipsometry begins to fail as the material becomes transparent (near 1700 nm), while the R/T method remains a powerful tool for determination of the near-bandgap optical constants.

'The Layer Matrix'). For this sample, the nonlinear least-squares algorithm used to determine $N^*(\lambda)$ would not converge in the fully transmissive (sub-bandgap) region. The results in the partially transmissive region seem reasonable, however, and the data have been used to calculate the $\text{In}_{0.53}\text{Ga}_{0.47}\text{As}$ bandgap in figure 16. The plot uses the allowed transition, direct-bandgap form for absorption (19, 20):

$$\alpha \propto \frac{(E - E_g)^{0.5}}{E}$$

where:

$$\alpha = 4\pi k/\lambda$$

to determine E_g (the x-intercept of $(\alpha E)^2$ vs. E).

The raw reflectance and transmittance data are presented in figure 17, and they show the strong interference fringes characteristic of a thin, planar structure. The diffuse reflectance of the sample was measured with an integrating sphere (up to the 2000 nm wavelength limit of the sphere), and the data are also shown in figure 17. The results indicate that the sample is extremely specular (<2% diffuse component). The characteristics of specular, planar structures will be explored in the following chapter on the modeling of multi-layered solar cells.

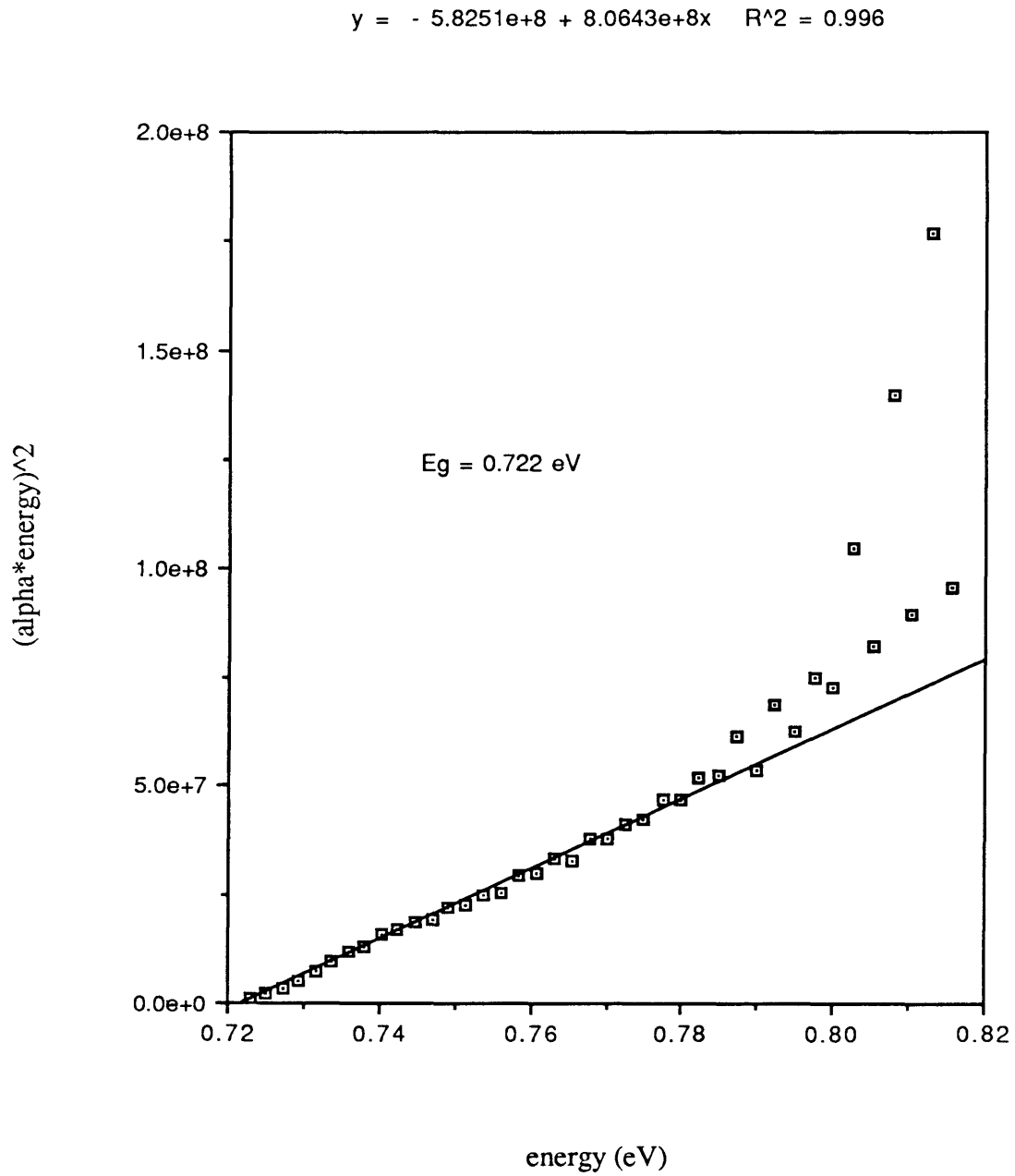


Figure 16. $(\alpha E)^2$ vs. E for the raw data of figure 17. The x-intercept gives the bandgap of $\text{In}_{0.53}\text{Ga}_{0.47}\text{As}$: $E_g = 0.722 \pm 0.001 \text{ eV}$. Data at energies less than 0.780 eV were used in the least squares fit.

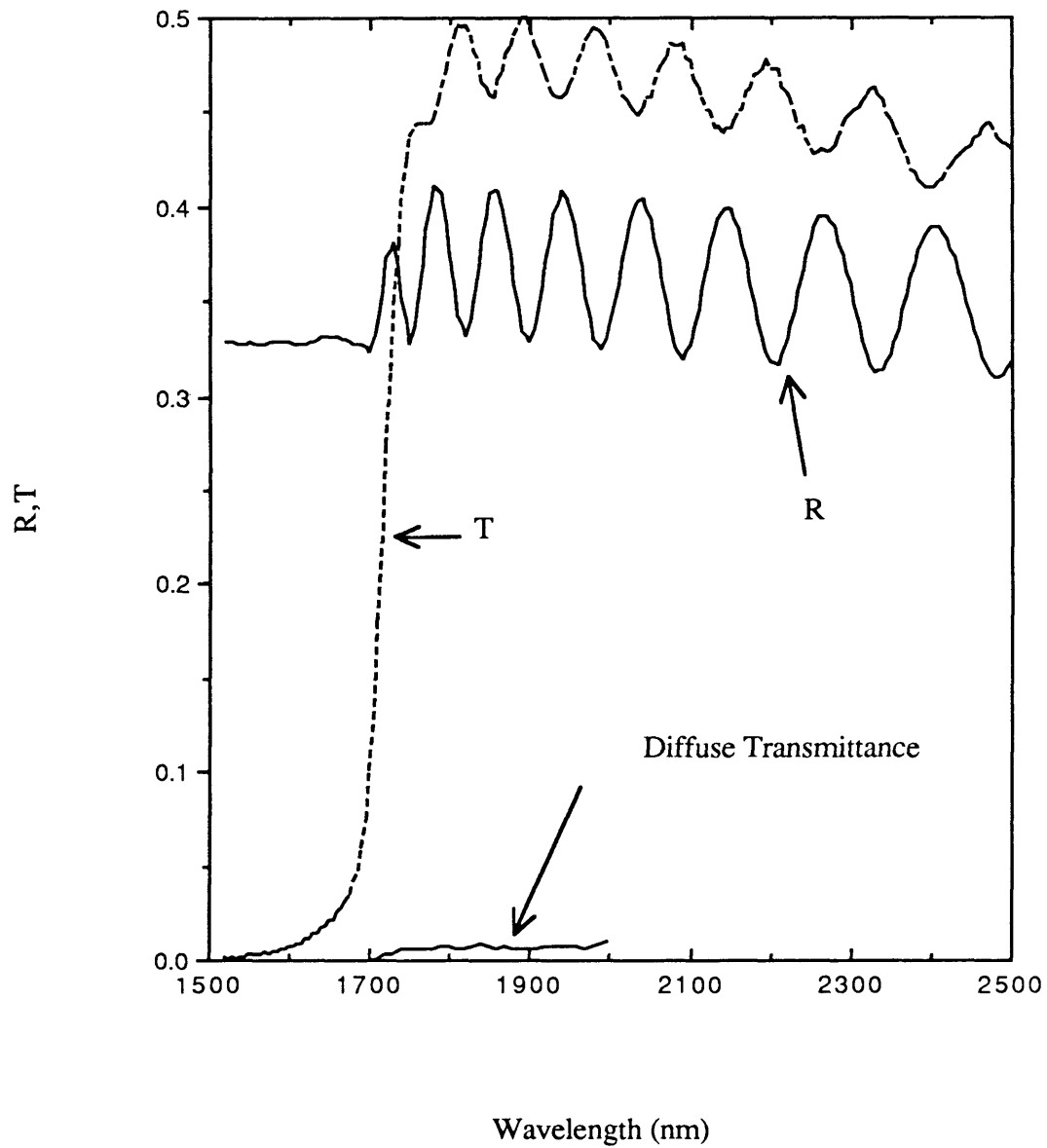


Figure 17. Reflectance, transmittance and diffuse transmittance of an $\text{In}_{0.53}\text{Ga}_{0.47}\text{As}$ film on an InP substrate.

Chapter 4

MODELING

The optical constants of a material may be used to design optimized optoelectronic devices. Specifically, this chapter uses the results of chapter II ($N^*(\lambda)$ of several III-V compounds) to design antireflection coatings for several high-efficiency solar cells. State-of-the-art solar cells using InP, indium tin oxide (ITO), $\text{In}_{0.53}\text{Ga}_{0.47}\text{As}$ and $\text{In}_{0.25}\text{Ga}_{0.75}\text{As}_{0.54}\text{P}_{0.46}$ have recently been grown at SERI. Optimization of antireflection coatings (ARCs) for these cells should further improve performances.

4.1. Short Circuit Current Optimization

Qualitatively, the minimization of reflectance is required for maximum current output from a solar cell. However, the incident spectrum and internal quantum efficiency must also be included to properly weight the result and obtain the relevant figure of merit for J_{sc} . The short circuit current of a solar cell may be calculated according to the relation (21):

$$J_{sc} = e \int_0^{\infty} \frac{I(\lambda) \times QE_{ext}(\lambda)}{(1 - R(\lambda))} \times (1 - R'(\lambda)) d\lambda \quad (4.1)$$

J_{sc} = short circuit current (Amp cm^{-2})

$I(\lambda)$ = incident spectrum (photons $\text{nm}^{-1} \text{cm}^{-2} \text{sec}^{-1}$)

λ = wavelength (nm)

e = electronic charge (Amp second)

$QE(\lambda)$ = external quantum efficiency (electrons photon^{-1})

$R(\lambda)$ = cell reflectance before ARC application (dimensionless)

$R'(\lambda)$ = calculated cell reflectance for specific ARC geometry (dimensionless)

$I(\lambda)$ is usually selected from the available ASTM standards (global, AM0, direct, etc.) (22) according to the projected operating conditions of the solar cell. This thesis uses only the direct (ASTM E891-82) incident spectrum (figure 18), consistent with concentrator designs.

The external quantum efficiency of the devices is measured at SERI with standardized methods (23). The uncoated cell reflectance ($R(\lambda)$) is measured with the CARY 2300 spectrophotometer described in chapter III. The only computational quantity in equation 4.1 is $R'(\lambda)$, the reflectance after the application of multiple ARCs. $R'(\lambda)$ is a continuous function of the thicknesses and indices of the ARCs, and thus it must be calculated separately for each J_{sc} integration. In practice, several parameters (typically ARC thicknesses) are systematically varied to maximize J_{sc} for a particular solar cell configuration.

Closed form solutions exist for reflectance from one, two and three-layer systems (12, 18), but the equations quickly become unwieldy for more complex optical stacks. The J_{sc} integral requires calculation of $R'(\lambda)$ for an arbitrary, multiple-layer optical stack,

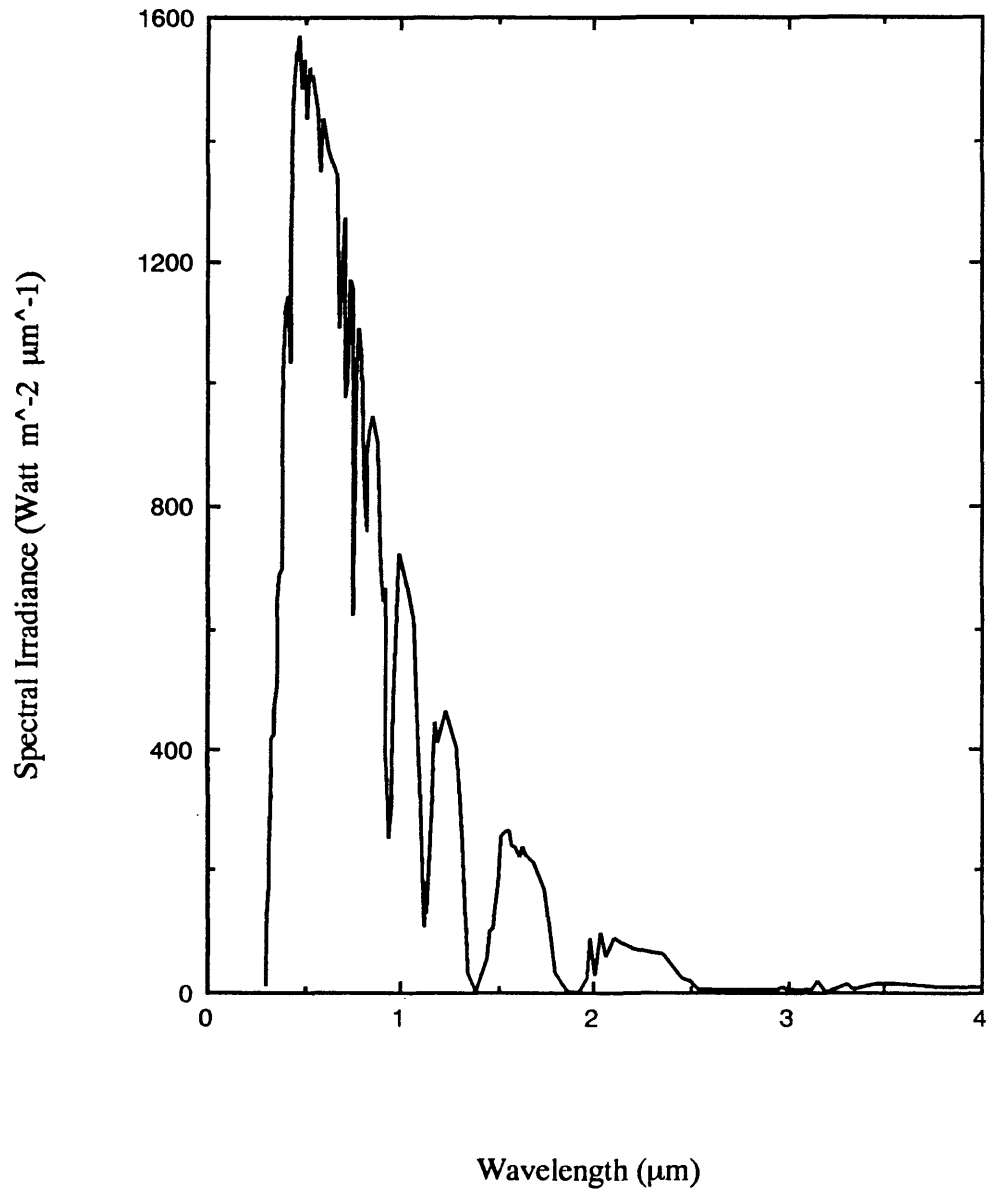


Figure 18. Global irradiance spectrum used in the modeling of the short-circuit current (ASTM-E891-82).

but the expression need not be in closed form. The method of Abeles (10) uses a scattering matrix formalism to achieve such a result.

4.2. The Scattering Matrix Method

This method for the calculation of reflectance and transmittance from an n-layer optical stack assumes homogeneous, linear media and plane wave incident electric fields. The electric field at any point in the medium may be decomposed into forward and backward-travelling waves designated E^+ and E^- , respectively (18, 24). The linear properties of the medium dictate that fields at arbitrary planes z and z' (figure 17) be related by a 2x2 matrix transformation, S (12):

$$E(z) = \underline{S} E(z')$$

S , the total electric field scattering matrix, is constructed according to the specific geometry and indices of refraction of the device. Field matching conditions are applied at each interface, and wave propagation is described through each material.

4.2.1 The Interface Matrix, I

Consider an isolated planar interface as pictured in figure 19a (12). Planes z and z' are placed arbitrarily close to the interface so that the 2x2 transformation matrix from z to z'

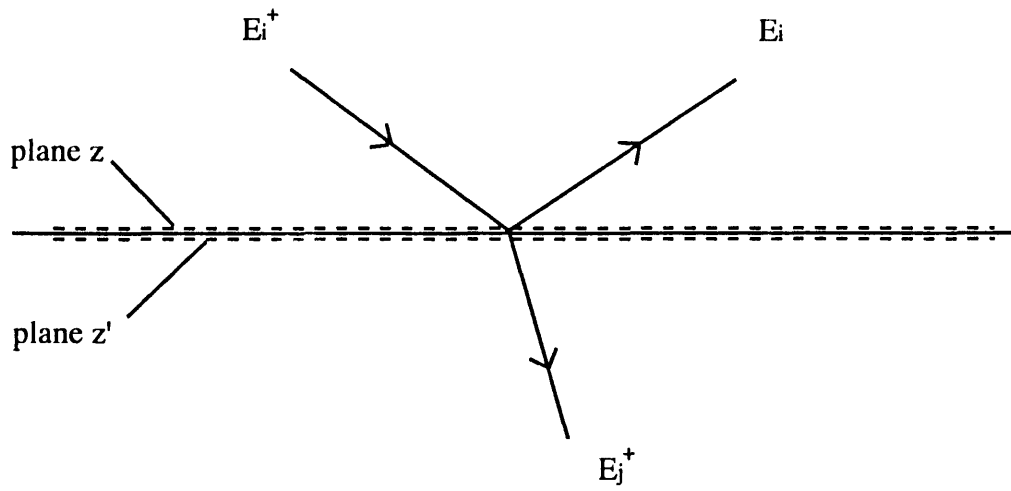


Figure 19a. Arrangement of the planes z and z' for derivation of the interface matrix, I .

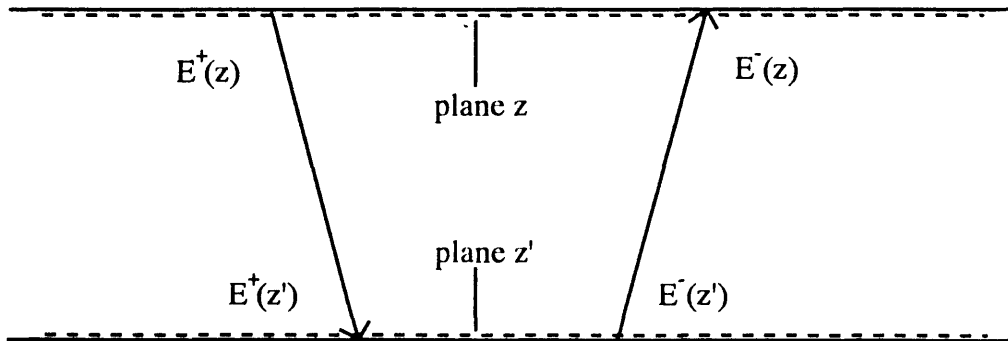


Figure 19b. Arrangement of the planes z and z' for derivation of the layer matrix, L .

describes only interface properties. This is a single-event plane wave scattering process, so only three waves (incident, reflected, and transmitted) have non-zero amplitudes. By inspection, without explicitly determining the transform matrix elements I_{ij} , the transform may be written:

$$\begin{bmatrix} E_i^+ \\ E_i^- \end{bmatrix} = \begin{bmatrix} I_{11} & I_{12} \\ I_{21} & I_{22} \end{bmatrix} \begin{bmatrix} E_j^+ \\ 0 \end{bmatrix}$$

Or, in equation form:

$$E_i^+ = I_{11} E_j^+ \quad (4.2)$$

$$E_i^- = I_{21} E_j^+ \quad (4.3)$$

The Fresnel equations (1.1-1.4) for dielectric media interfaces explicitly determine the r_{ij} and t_{ij} . By definition:

$$E_j^+ = t_{ij} E_i^+ \quad (4.4)$$

$$E_i^- = r_{ij} E_i^+ \quad (4.5)$$

Comparison of equation 4.2 and 4.4 reveals that:

$$I_{11} = \frac{1}{t_{ij}} \quad (4.6)$$

Equation 4.3 may be rewritten:

$$\begin{aligned} E_i^- &= I_{21} \frac{E_i^+}{I_{11}} \\ \therefore E_i^- &= I_{21} t_{ij} E_i^+ \end{aligned} \quad (4.7)$$

Comparison with equation 4.5 yields:

$$\begin{aligned} I_{21} t_{ij} &= r_{ij} \\ \text{or } I_{21} &= \frac{r_{ij}}{t_{ij}} \end{aligned} \quad (4.8)$$

Similar manipulations permit explicit representation of all of the interface matrix elements in terms of the Fresnel coefficients (12):

$$I_{-i,j} = \begin{bmatrix} \frac{1}{t_{ij}} & \frac{r_{ij}}{t_{ij}} \\ \frac{r_{ij}}{t_{ij}} & \frac{1}{t_{ij}} \end{bmatrix} \quad (4.9)$$

As expected, the interface matrix depends only on the complex electric field reflection and transmission coefficients.

4.2.2. The Layer Matrix, \mathbf{L}

Next, consider a single, homogeneous, linear medium delimited by two planar interfaces. Planes z and z' are placed just inside of the interfaces, as in figure 19b. In the case of a linear medium, the matrix which describes propagation and attenuation from z to z' does not mix forward and backward travelling waves (i.e.- the matrix is diagonal) (12, 18, 24):

$$\begin{bmatrix} E^+(z) \\ E^-(z) \end{bmatrix} = \begin{bmatrix} L_{11} & 0 \\ 0 & L_{22} \end{bmatrix} \begin{bmatrix} E^+(z') \\ E^-(z') \end{bmatrix}$$

The form of the diagonal elements is a result of the (assumed) plane wave nature of the electric field. The amplitude of the 'forward travelling' component at the point z' is (sinusoidal time dependence $e^{+i\omega t}$ is implicit) (5):

$$\begin{aligned} E^+(z') &= E^+(z)e^{-iq^*x} \\ &= E^+(z)e^{-iqx \cos(\phi)} \\ &= E^+(z)e^{-i\frac{N^* \omega}{c}x \cos(\phi)} \\ &= E^+(z)e^{-i\frac{2\pi N^*}{\lambda}x \cos(\phi)} \end{aligned}$$

Where \mathbf{q} is the incident light wave-vector, x is the distance between planes z and z' , ϕ is the local angle of incidence and $N^*=N-ik$. The previous equation may be solved for $E^+(z)$:

$$E^+(z) = E^+(z')e^{i\frac{2\pi N^*}{\lambda}x \cos(\phi)}$$

and similarly, for the backward travelling wave ($q \rightarrow -q$):

$$E^-(z) = E^-(z')e^{-i\frac{2\pi N^2 x \cos(\phi)}{\lambda}}$$

Using these results, the layer matrix may be written:

$$L_j = \begin{bmatrix} e^{i\beta_j} & 0 \\ 0 & e^{-i\beta_j} \end{bmatrix} \quad (4.10)$$

thus defining the "phase thickness," β :

$$\beta_j = \frac{2\pi N_j^2 d_j \cos(\phi_j)}{\lambda} \quad (4.11)$$

d_j = jth layer thickness (nm)

ϕ_j = local angle of incidence for jth layer

λ = wavelength of light (nm)

The propagation of light (wavelength= λ) through an optical layer thus depends only on the local index of refraction, angle of incidence and the layer thickness.

4.2.3. The Total Scattering Matrix for Coherent Lamella

A stratified medium may be described by a series of alternating interface and layer matrices (as described above). The layers must be planar and parallel to fit this 'lamelliform' model (24). Standard matrix multiplication yields the total electric field scattering matrix for an m-layer structure in terms of the **I** and **L** matrices:

$$\mathbf{S} = \mathbf{I}_{0,1} \mathbf{L}_{-1,-1,2} \mathbf{I}_{-1,-1,2} \mathbf{L}_{-2} \dots \mathbf{L}_{-m-1,-m-1,m} \mathbf{I}_{-m-1,-m-1,m}$$

The implicit assumption is that there is no reflection from the back side of the mth layer. Usually, the mth layer is the exit medium, although the condition of no back-surface reflection may also be met by a sufficiently absorptive layer in the structure. This assumption may be cast in matrix form (figure 20) (12):

$$\begin{bmatrix} \mathbf{E}_1^+ \\ \mathbf{E}_1^- \end{bmatrix} = \begin{bmatrix} \mathbf{S}_{11} & \mathbf{S}_{12} \\ \mathbf{S}_{21} & \mathbf{S}_{22} \end{bmatrix} \begin{bmatrix} \mathbf{E}_m^+ \\ 0 \end{bmatrix}$$

or:

$$\mathbf{E}_1^+ = \mathbf{S}_{11} \mathbf{E}_m^+ \quad (4.12)$$

$$\mathbf{E}_1^- = \mathbf{S}_{21} \mathbf{E}_m^+ \quad (4.13)$$

The total (complex) reflectance and transmittance are defined:

$$\tilde{r} = \frac{\mathbf{E}_1^-}{\mathbf{E}_1^+} \quad (4.14)$$

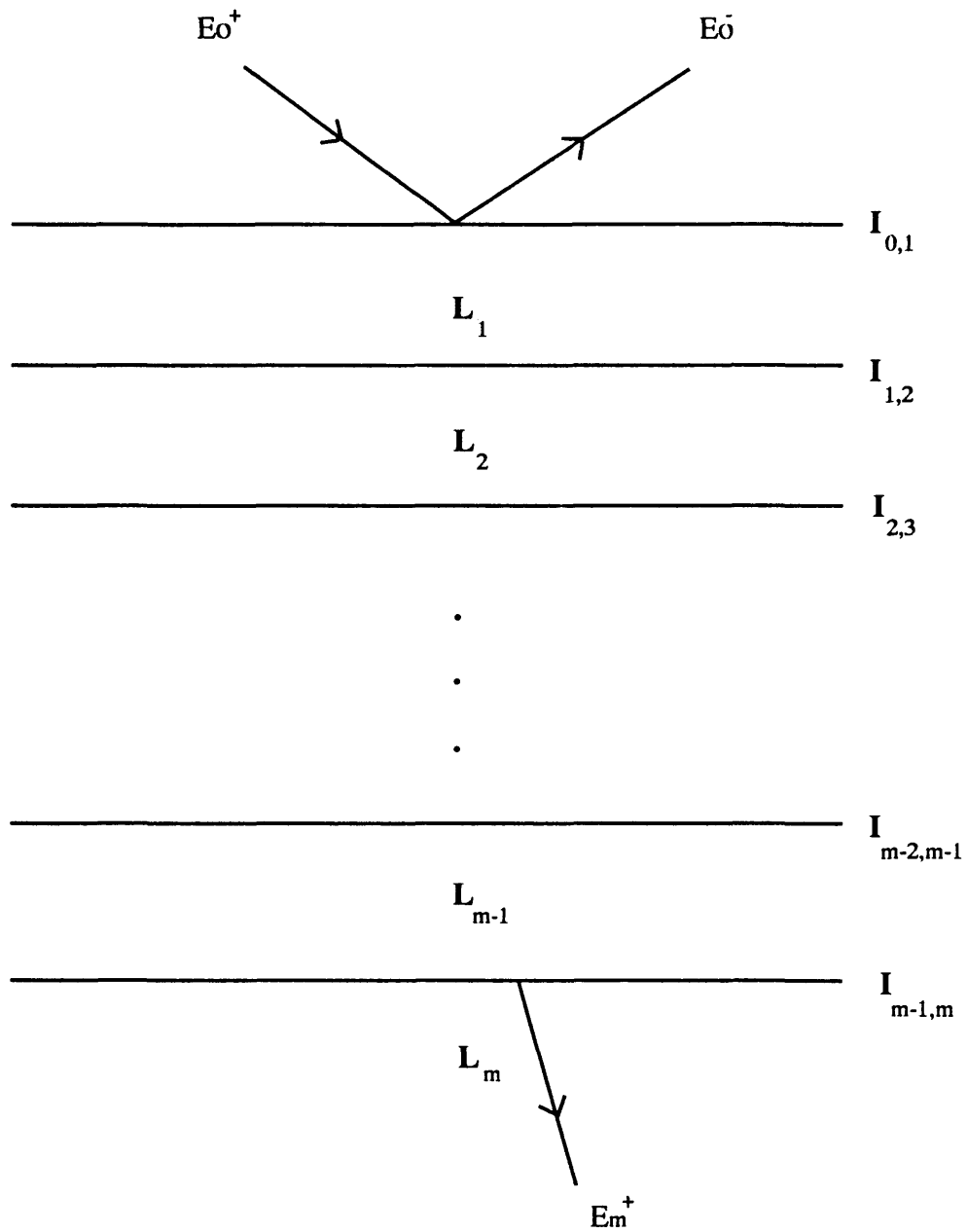


Figure 20. Construction of an m -layer optical stack with the appropriate interface and layer matrices.

$$\tilde{t} = \frac{E_m^+}{E_1^+} \quad (4.15)$$

Combination of equations 4.12, 4.13 and 4.14 yields:

$$\tilde{r} = \frac{S_{21}}{S_{11}}$$

while equations 4.15 and 4.12 give:

$$\tilde{t} = \frac{E_m^+}{E_1^+} = \frac{1}{S_{11}}$$

Explicit calculation of the scattering matrix elements thus yields the measurable reflectance and transmittance (the asterisks denote the complex conjugate):

$$R = |\tilde{r}|^2 = \left(\frac{S_{21}}{S_{11}}\right)^* \left(\frac{S_{21}}{S_{11}}\right)$$

$$T = |\tilde{t}|^2 = \left(\frac{1}{S_{11}}\right)^* \left(\frac{1}{S_{11}}\right)$$

4.3. Computer Implementation

The previous section described the matrix method of reflectance calculation for a fixed m-layer geometry and single wavelength. This calculation must be iterated at many wavelengths to generate the discretized function $R'(\lambda)$ which is necessary for numerical integration of equation 4.1. The entire process is repeated for all variations in ARC thickness to generate a contour plot of J_{SC} , and it is thus quite computer intensive.

The method requires 2x2 matrix routines for complex numbers. Special complex number-handlers have been written in the Pascal programming language to facilitate these calculations. The code is in a separately compiled unit (similar in function to a Fortran library), and all of the procedures and complex number definitions are available when this unit is referenced by a Pascal program.

4.4. Comparison of Measured and Modeled Reflectance

The matrix method described in the previous sections uses the standard lamelliform definition: plane-parallel slabs of homogeneous dielectric media. Actual samples approximate this model in varying degrees according to the growth conditions and individual deposition techniques. Therefore, it is imperative that the model's applicability be tested before confidence can be placed in the final calculated J_{SC} results. The test is simple, direct, and it combines all of the techniques developed in this thesis.

The optical constants of a material are first measured with the wavelength scanning ellipsometer. The data are used in the matrix method calculation to generate a 'predicted'

reflectance curve. The reflectance is then measured directly with the Cary 2300 spectrophotometer, and the degree of agreement between the measured and modeled reflectance spectra indicates the applicability of the model and/or accuracy of the measurement techniques.

Figure 21 shows a comparison of measured and modeled reflectance for $\text{In}_{0.25}\text{Ga}_{0.75}\text{As}_{0.54}\text{P}_{0.46}$. The curves agree to within 3 percent over the entire spectral range. No attempt was made to remove surface oxides before the reflectance measurement, and the reflectance uncertainty is usually quoted as being $\pm 3\%$ due to sample positioning sensitivity. Thus, the predicted and measured reflectance show very good agreement to within experimental uncertainties. This verifies the applicability of the lamelliform model for the samples in this study.

4.5. Modeling Results

The short-circuit current (equation 4.1) is, in general, a function of several solar cell parameters (quantum efficiency, layer thicknesses and indices of refraction). In practice, a given solar cell is grown which exhibits a specific quantum efficiency ($\text{QE}(\lambda)$) and uncoated reflectance ($\text{R}(\lambda)$). Two-layer antireflection coatings are standard in the solar cell industry, and the selection of materials is often quite limited (MgF_2 , ZnS , Al_2O_3 , etc.). Thus, the optimization of the short-circuit current for a specific solar cell reduces to optimization of the two ARC thicknesses.

This problem lends itself to presentation in a contour graph format (c.g.- figure 22). Each axis corresponds to the thickness of one ARC, and the data is presented as discretized

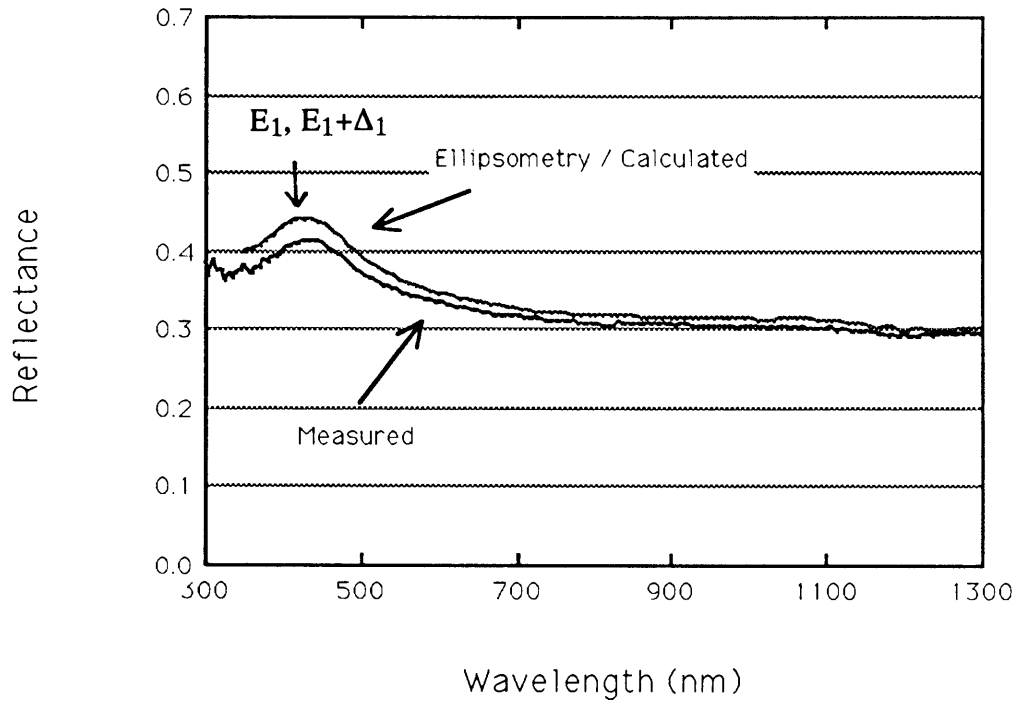


Figure 21. Comparison of the predicted and measured reflectance of $\text{Ga}_{0.25}\text{In}_{0.75}\text{As}_{0.54}\text{P}_{0.46}$. The predicted spectrum was generated from ellipsometrically determined $N^*(\lambda)$ and the lamelliform computer model described in the text.

lines of constant J_{sc} . From the graph, optimal ARC thicknesses are easily correlated to the maximum J_{sc} . $N^*(\lambda)$ values for MgF_2 and ZnS were measured with the R/T method described in chapter 3 (25).

A J_{sc} contour plot for the structure (top to bottom:) $*MgF_2/*ZnS/MgF_2(2nm)/InP$ is shown in figure 22. The asterisk denotes a layer whose thickness is variable. All other layer thicknesses are held constant. The 2 nm MgF_2 layer is often deposited directly on the InP to enhance ZnS nucleation characteristics, and so it is included in the optical model for completeness. Optimal MgF_2 and ZnS thicknesses are determined to be $\sim 95nm$ and $\sim 55nm$, respectively.

It is extremely time-consuming to experimentally verify a two-dimensional J_{sc} contour plot, since each data point represents an individually coated solar cell. However, the confidence level in these results would be raised significantly through some type of verification. This exercise has been completed for the indium tin oxide/ indium phosphide (ITO/ InP) solar cell.

Figure 23 shows the J_{sc} contour results for the structure $*MgF_2/*ITO/InP$. In this case, the ITO acts as the sandwiched ARC, while MgF_2 is used as the top ARC. This particular application requires several approximations, since the ITO is an integral (conducting) part of the solar cell. It is assumed that the quantum efficiency is independent of ITO thickness (an assumption which will certainly fail for significantly thinner ITO). The results are, however, valid for a broad range of ITO thicknesses centered on 60 nm, since the external quantum efficiency and reflectance data were obtained from such a device.

The model predicts that the maximum J_{sc} will occur with a ~ 70 nm MgF_2 coating on top of the ITO/ InP cell. The uncoated ITO/ InP structure was cleaved into nine samples,

each with a small solar cell intact. The ITO thickness for each cell was measured with ellipsometry (all thicknesses were near 55 nm), and MgF₂ coatings were individually applied with thicknesses which vary between 0 and 170 nm. These thicknesses were also measured ellipsometrically.

Short-circuit currents were measured for each cell, and the results are compared in figure 24 to the values predicted in figure 23. The predicted curve has been normalized to the experimental uncoated J_{SC} , since relative, rather than absolute quantum efficiency was used in the integration of equation 4.1. This normalization does not affect the accuracy of the predicted optimum ARC thickness.

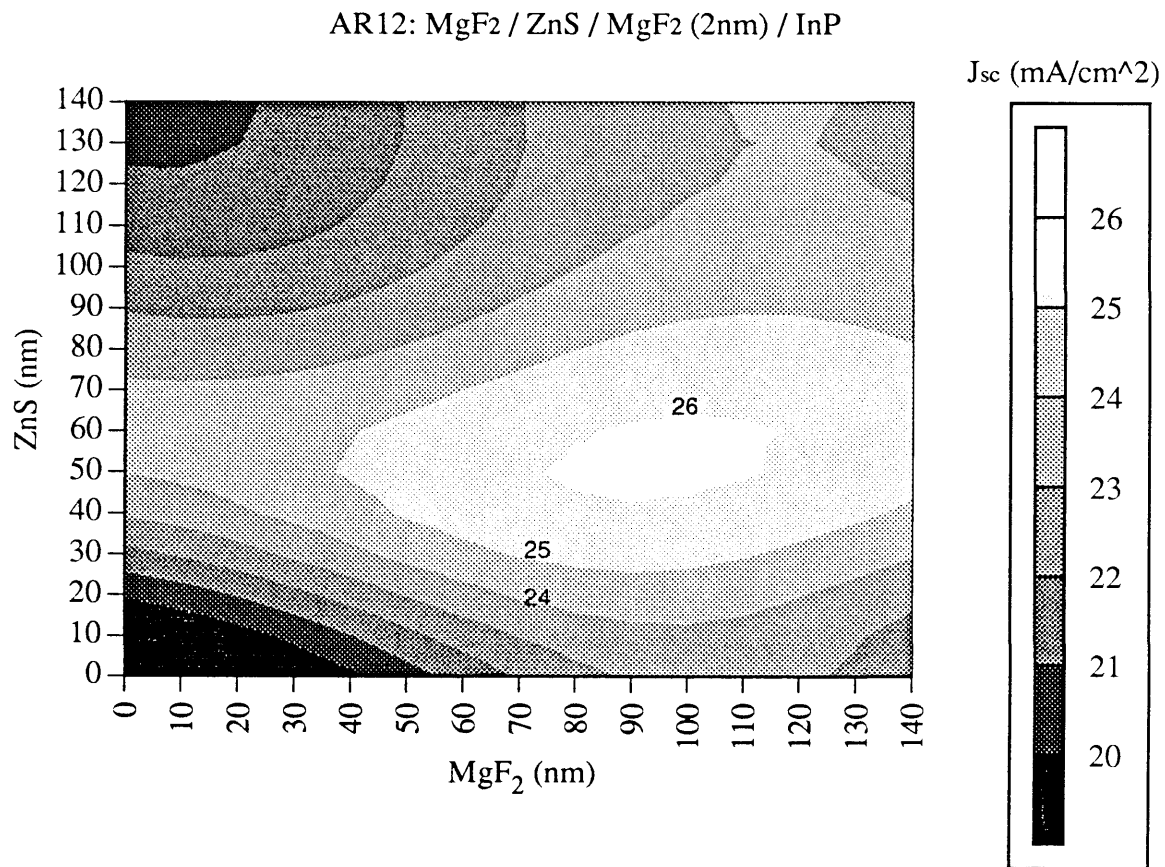


Figure 22. Short circuit current of an InP homojunction as a function of the thicknesses of ZnS and MgF₂. A nucleating layer of MgF₂ (2 nm thick), which is necessary for proper growth on ZnS on InP, is included in this model. Optimal ARC thicknesses are as follows: ZnS = ~55 nm, MgF₂ = ~95 nm.

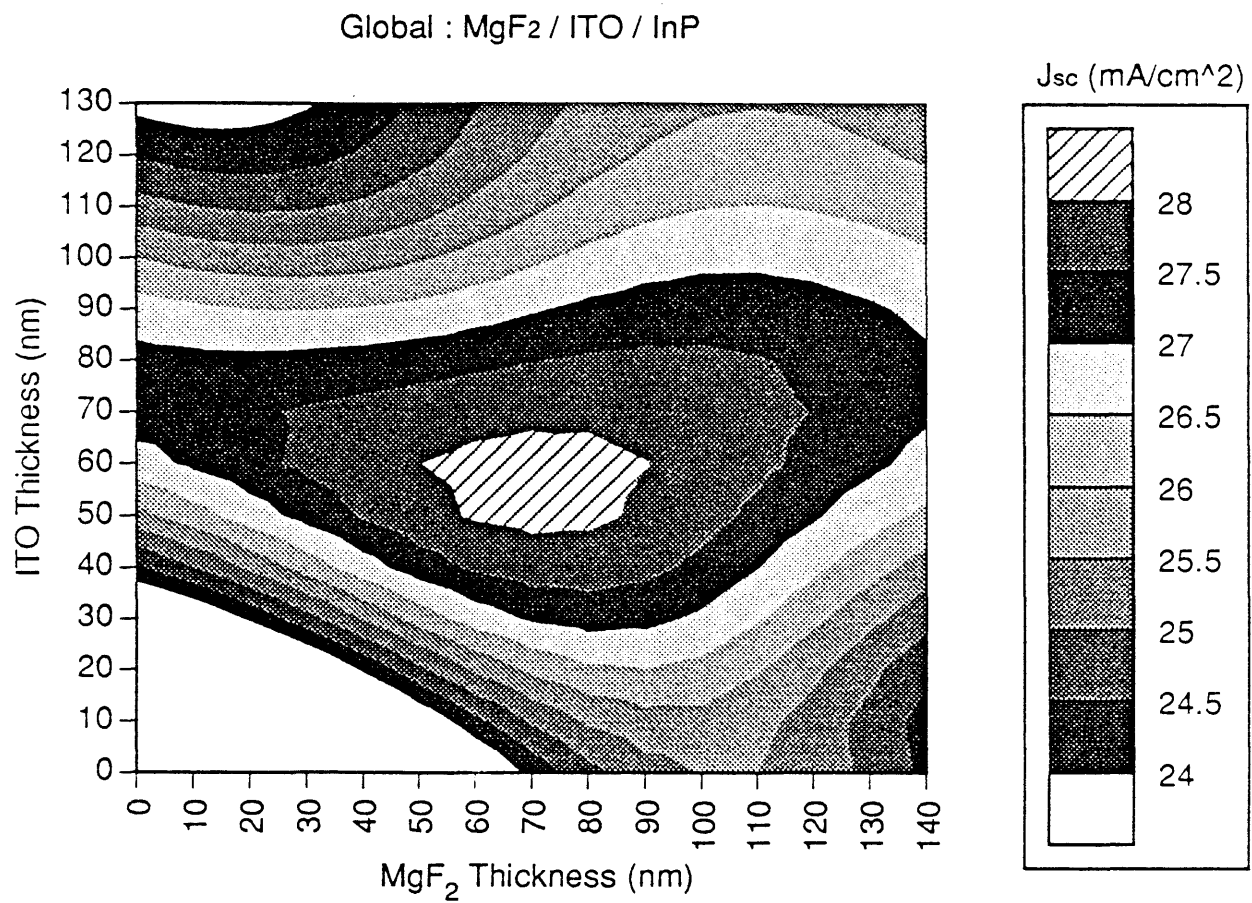


Figure 23. Short-circuit current contour plot for the structure *MgF₂/*ITO/InP. Optimal ARC thicknesses are as follows: MgF₂ = ~70 nm, ITO = ~55 nm.

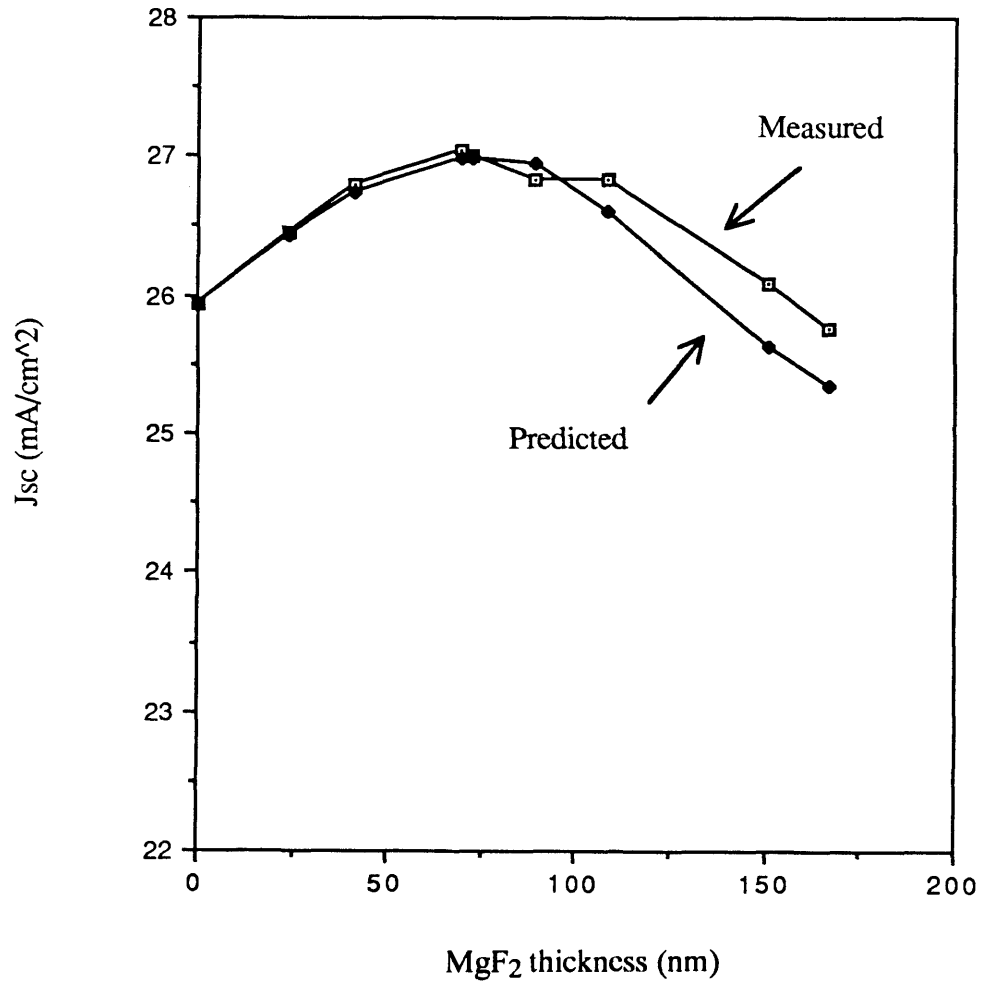


Figure 24. Comparison of predicted and experimentally determined short-circuit currents for the structure of figure 23. The MgF_2 thickness was varied from 0-170 nm while the ITO thickness was kept essentially constant at ~ 55 nm.

Chapter 5

CONCLUSIONS

The emphasis of this thesis has been on the development of a new visible-near infrared wavelength scanning ellipsometer. The system has been fully automated, and the initial results show close agreement with other published data in the visible portion of the spectrum (figure 12). Near infrared ellipsometric data are not available for comparison, but consistency checks such as the comparison of modeled and measured reflectance (figure 21) show that the data exhibit good accuracy.

Sample preparation is extremely important in ellipsometry, since the technique is primarily a surface probe. The use of lattice-matched capping layers which exhibit significantly different etch rates from the underlying sample has proved to be an important tool in surface oxide elimination. The overlying layer is removed just prior to the measurement, providing an abrupt surface for measurement. Results indicate that this method provides a cleaner surface than any of the standard chemomechanical surface pretreatments.

The magnitude of the imaginary part of the dielectric function at an energy corresponding to a band-to-band transition is often used as a measure of surface quality. A higher peak in ϵ'' indicates a more abrupt and contaminant-free surface. The techniques employed in this study have yielded peak heights which compare favorably with those in the literature, and even exceed published values, particularly when the lattice-matched capping technique is used.

Comparison of measured $\epsilon''(E_1, E_1+\Delta_1)$ peak heights with those in the literature.

	SERI Peak Height	Literature Peak Height (3)
InP	17.36 @ 400 nm	~17 @ 400 nm
In _{0.53} Ga _{0.47} As	18.57 @ 480 nm (E_1)	~16 @ 420 nm ($E_1+\Delta_1$)
In _{0.25} Ga _{0.75} As _{0.55} P _{0.45}	15.47 @ 420 nm	~15 @ 413 nm

Ellipsometrically determined $N^*(\lambda)$ data for several members of the InGaAsP alloy system have been used to optimize antireflection coatings for several high-efficiency solar cells. Optical constants for the transparent antireflection coatings which were used in this work were determined by R. Dhere in a separate reflectance/transmittance study (25). A computer model has been developed which calculates the short-circuit current for an n-layer solar cell, given the quantum efficiency, incident spectrum, and uncoated cell reflectance. The calculated optimal ARC layer thicknesses are not surprising (they approximate the quarter wave optical thicknesses), but the ability to generate a J_{sc} contour plot has revealed that the current density maxima are reasonably insensitive to the individual layer thicknesses. This relaxes the ARC deposition constraints, and shows that the short-circuit current will not degrade significantly, even with a layer thickness deposition precision of ± 10 nm.

REFERENCES

1. B. Streetman, Solid State Electronic Devices, 3rd edition, Prentice Hall, Englewood Cliffs, New Jersey (1990).
2. R.E. Nahory, et al, "Band Gap Versus Composition and Demonstration of Vegard's Law for $\text{In}_{1-x}\text{Ga}_x\text{As}_y\text{P}_{1-y}$ Lattice Matched to InP," *Phys. Rev. B*, 33, 7, p. 659 (1978).
3. S. Adachi, "Optical Properties of $\text{In}_{1-x}\text{Ga}_x\text{As}_y\text{P}_{1-y}$ Alloys," *Phys Rev. B*, 39, 17, pp. 12,612-12,621 (1989).
4. M.W. Wanlass et al, "Development of High-Performance GaInAsP Solar Cells for Tandem Solar Cell Applications," *Proceedings of the Twenty First IEEE Photovoltaic Specialists Conference*, pp. 172-175 (1990).
5. D.E. Aspnes, "Analysis of Modulation Spectra of Stratified Media," *Journal of Opt. Soc. of America*, 63, p. 1380, 1973.
6. S.G. Lipson and H. Lipson, Optical Physics, Cambridge U. Press, 1981.
7. D.E. Aspnes and Y. Petroff in Handbook On Semiconductors 2, T.S. Moss, editor, North-Holland, Amsterdam (1980).
8. R.W. Collins and Y. Kim, "Ellipsometry for Thin-film and Surface Analysis," *Analytical Chemistry*, 62, 17, p. 887 (1990).
9. D.E. Aspnes, "The Characterization of Materials by Spectroscopic Ellipsometry," SPIE vol. 452, *Spectroscopic Characterization Techniques for Semiconductor Technology* (1983).
10. F. Abeles, "On the Propagation of Electromagnetic Waves in Stratified Media." *Ann. de Physique*, 12, 3, pp. 504-520 (1948).
11. J.D. Jackson , Classical Electrodynamics, 2nd edition, John Wiley and Sons, New York (1975).
12. Azzam and Bashara, Ellipsometry and Polarized Light, 1st edition, North-Holland Publishing Co. (1977).
13. J. A. Woollam, P.G. Snyder, and W.A. McGahan, "Fundamentals and Applications of Ellipsometry-1990," Text for short course at University of Nebraska, Lincoln (1990).
14. D.E. Aspnes and A.A. Studna, "Chemical Etching and Cleaning Procedures for Si, Ge, and some III-V Compound Semiconductors," *Applied Physics Letters*, 39, 4, p. 316 (1981).

15. M. Erman and J.B. Theeten, "Analysis of Ion-Implanted GaAs by Spectroscopic Ellipsometry," *Surface Science* 135, pp. 353-373 (1983).
16. E.D. Palik, ed., Handbook of Optical Constants of Solids, Academic Press (1985).
17. H. Burkhard, H.W. Dinges, and E. Kuphal, "Optical Properties of $\text{In}_{1-x}\text{Ga}_x\text{P}_{1-y}\text{As}_y$, InP, GaAs, and GaP Determined by Ellipsometry," *Journal of Applied Physics*, 53, 1, (1982).
18. W. Heavens, "Optical Properties of Thin Solid Films," Academic Press, New York (1955).
19. W. Kowalsky et al, "Optical Absorption and Refractive Index Near the Bandgap for InGaAsP," *Phys. Stat. Sol. (a)*, 77, p. 75 (1983).
20. J. Pankove, Optical Processes in Semiconductors, Dover (1975)
21. H.J. Hovel, "Solar Cells," in R.K. Willardson and A.C. Beer (eds.), Semiconductors and Semimetals, Vol. 11 (1975).
22. K.A. Emery and C.R. Osterwald, "Efficiency Measurements and Other Performance-Rating Methods," Current Topics in Photovoltaics, Vol. 3, Chap. 4, Academic Press (1988).
23. T.J. Coutts and C.R. Osterwald, "The Quantum Efficiency of CdS/CuInSe₂ and In₂O₃:Sn/InP Solar Cells," Solar Cells, 22, pp. 195-209 (1987).
24. R.F. Potter, in Handbook of Optical Constants of Solids, E.D. Palik, editor, Academic Press (1985).
25. R. Dhere, private communication, July, 1990.